Journal of Wind Engineering & Industrial Aerodynamics 241 (2023) 105500

Contents lists available at ScienceDirect

Journal of Wind Engineering & Industrial Aerodynamics

journal homepage: www.elsevier.com/locate/jweia

A simplified CFD approach for bluff-body aerodynamics under small scale free stream turbulent flow

Antonio J. Álvarez [a], Félix Nieto [a,*], Kenny K.C.S. Kwok [b], Santiago Hernández [a]

[a] CITEEC, University of A Coruña, Spain
[b] School of Civil Engineering, The University of Sydney, Australia

ARTICLE INFO

Keywords:
Free stream turbulence
Small-scale turbulence
Bluff body
2D URANS
Rod
Square
K-ω SST

ABSTRACT

The study of free stream turbulence (FST) effects on bluff bodies by means of computational approaches has been addressed so far mainly applying scale resolving methods adopting a three-dimensional domain, which is cumbersome and complex. The development of an alternative more affordable approach capable of providing reliable data, at least qualitatively, about the impact of FST in aerodynamic responses of interest would be very beneficial for the penetration of CFD techniques in industrial applications. In this work, a 2D URANS approach is adopted to numerically replicate the well-known rod-induced small scale turbulent flow in wind tunnel testing. A square cylinder is selected as canonical application case to study the effects caused by ambient turbulence (0.7%), and 3.3% and 6.8% FST levels. The numerical results for the force coefficients, base pressure coefficient, mean and fluctuating pressure coefficient distributions, time-averaged flow structures, mean streamwise velocity and Reynolds stresses distributions are reported along with experimental data in the literature for exhaustive validation. The agreement between the proposed CFD approach and the wind tunnel data is remarkable as not only qualitative agreement has been reached, but in many cases consistency between numerical and experimental data has been obtained. The proposed approach, once its feasibility and accuracy has been satisfactorily assessed, may be applied for affordably study FST-dependent aerodynamics problems of interest in wind engineering.

1. Introduction

The turbulent nature of the atmospheric boundary layer explains the need for considering turbulent incoming flow in wind engineering studies as this might play a crucial role in the aerodynamics of bluff bodies. The traditional approach to analyze the effects of free stream turbulence consists of conducting wind tunnel tests manipulating the incoming flow to reach targeted turbulent characteristics. In general, the first option consists of placing a passive grid located upstream of the studied model, controlling the turbulent characteristics, such as turbulent intensity and length scale, via grid openness and bars size, as well as the downwind distance from the studied model (see Vita et al., 2018, for more comprehensive details and description of variants). Alternatively, boundary layer wind tunnels have been used to mimic atmospheric turbulent flow profiles using spires located at the inlet, roughness blocks placed over the floor along the wind tunnel, or castellated barriers, which enhance the turbulent content as the flow develops along the fetch of the wind tunnel (see for instance Farell and Iyengar, 1999; Kozmar and Laschka, 2019, among others).

The fundamental role in bluff body aerodynamics played by the turbulent characteristics of the incoming flow has been addressed since the early stages in aerodynamics research using experimental methods, as it has been explained in Lander et al. (2016), citing contributions published as early as 1929 and 1935. Nowadays, the literature on experimental studies about free stream turbulence effects on aerodynamic and aeroelastic responses is vast, encompassing basic changes in integral parameters, such as force coefficients or base pressure, as well as more fundamental topics, such as early transition in boundary layers, or separated shear layer development. However, computational wind engineering (CWE) applications addressing this topic in bluff body aerodynamics are in comparison scarce, in spite of the data management and visualization capabilities of Computational Fluid Dynamics (CFD). Focusing on the application case addressed herein, which is the canonical square prism under free stream turbulent flow, there is a large body of experimental studies such as Lee (1975), Nakamura and Ohya (1986), Saathoff and Melbourne (1989), McLean and Gartshore (1992),

* Corresponding author.
E-mail address: felix.nieto@udc.es (F. Nieto).

https://doi.org/10.1016/j.jweia.2023.105500
Received 29 November 2022; Received in revised form 26 June 2023; Accepted 2 July 2023
Available online 8 August 2023

Carassale et al. (2013), or Li et al. (2022), among many others. In all the cases, the turbulent flow has been generated by placing a grid upstream of the studied body. On the other hand, the references in the literature addressing numerical studies are scarce: Tamura and Ono (2003) applied a 3D Large Eddy Simulation (LES) model to study the static and oscillating square and a 2:1 ratio rectangular cylinder considering different levels of incoming turbulence; Noda and Nakayama (2003) also adopted a 3D LES approach for a square and a 2.5:1 rectangular cylinder in smooth and 5% turbulence intensity flows; Liu (2012) studied different variants in the 3D LES model formulation for a 5% turbulent intensity inflow; while Ranjan et al. (2017) included the heat transfer problem considering turbulent flow; Li et al. (2014) studied the effect of turbulence intensity and length scale in a rectangular tall building by LES, and Chen (2019) and Chen et al. (2020) studied by means of 3D LES simulations the impact of smooth and turbulent flow on the aerodynamics of a static and a oscillating square cylinder. Higher width to depth ratios have also attracted the attention of the computational wind engineering community recently. Some selected references studying 4:1 and 5:1 rectangular cylinders are Daniels et al. (2016), Ricci et al. (2017), or Zhu et al. (2020). In the selected references, the Synthetic Turbulence Method was applied to setup the turbulent inlet, covering a wide range of variants such as the Autoregressive Moving Average (ARMA) model in Liu (2012), or the Modified Discretizing and Synthesizing Random Flow Generation (MDSRFG) in Ricci et al. (2017), just to mention two of them.

It is the authors' opinion, the main reason for the limited number of computational studies on free stream turbulence effects on bluff body aerodynamics is the remarkable challenge posed by the definition of "*the inflow boundary of spatially developing turbulence simulations for which the accurate prescription of the incoming turbulent eddies as a function of time is a prerequisite to obtaining the unsteady solution in the interior of the domain*" (Wu, 2017); as well as the inherent computational burden of 3D LES simulations. Consequently, this issue has not been addressed in CFD practice with some success until the late 1990s and early 2000s (for instance, Lund et al., 1998; Klein et al., 2003, among several others). In Xing et al. (2022), the main issues that must be considered for the definition of turbulent inflow boundary conditions are reviewed, providing a comprehensive outlook that explains why this is still an active field of research. Available methods for scale resolved simulations, or hybrid RANS-LES, include the recycling method using wind tunnel data or numerically generated data (Mochida et al., 1993; Haque et al., 2014), and synthetic methods with several variants (Xie and Castro, 2008, Yu and Bay, 2014, Patruno and Ricci, 2018, Bervida et al., 2020, among several others). There have been proposals to define a turbulent inlet boundary condition in 3D URANS that could overcome the dissipation induced by the numerical formulation and the spatial discretization. For instance, in Balduzzi et al. (2019), a special method is proposed to setup a turbulent inlet akin to grid-induced turbulence. The approach requires developing a specific script defining the inlet velocity profile based on a Random Number Generator algorithm. To achieve the targeted turbulence properties, control variables associated to the mesh characteristics, the time discretization and the random number generation method should be considered. Furthermore, the method also requires the smoothing of flow discontinuities in time.

One conclusion that might be extracted from the existing literature dealing with the numerical definition of turbulent inflows is the complexity of the procedure, which depending on the adopted approach involve auxiliary simulations, generation of synthetic fields with target statistics and fulfilment of the Navier Stokes equations, or the application of the unsteady inflow conditions introducing modifications to avoid pressure fluctuations.

The above discussions highlight the need for an alternative approach that, at least, would enable qualitative prediction capabilities for CFD simulations in the frame of industrial applications or the preliminary assessment of the turbulence effects in the aerodynamic responses of interest in wind engineering. To this end, the current research resorts to the well-stablished rod-induced small-scale turbulence generation experimental procedure (Kwok and Melbourne, 1980; Kwok, 1986), implemented numerically herein by adopting a relatively inexpensive 2D URANS approach, combined with the nowadays standard in the field k-ω SST turbulence model. According to Gartshore (1973), the wake of the rod has roughly isotropic turbulence characteristics, and it is as effective as grid induced turbulence but more "*simple*" and "*convenient*". This approach has been adopted also in experimental research in Kiya and Sasaki (1983), and more recently in Lander et al. (2016). The purpose of this work is to develop a rigorous and cost-effective approach, based on verified spatial and temporal discretizations, assessing its merit by a comprehensive validation strategy with experimental data in the literature for a 0° angle of incidence square prism under rod-induced turbulent flow. It is noteworthy that two very different geometric scales, the one of the rod and the one of the square prism, are considered, which has required conducting independent verification studies of the fluid domain grids and time discretization for each geometry, applying the procedure proposed in Celik et al. (2008). Previous work by the authors on the subject has been reported in Alvarez et al. (2021), where preliminary basic results for smooth flow and 3.3% turbulence intensity level, adopting a first order implicit scheme in time, were published. In this article, smooth flow, 3.3% and 6.8% FST levels are studied in detail, adopting more demanding and accurate numerical settings, such as the second order backward scheme for advancement in time.

This research paper is organized as follows. In section 2 the basic formulation is reviewed, particularly the triple decomposition and turbulent intensity assessment; afterwards, the computational modeling approach adopted in this piece of research is introduced in section 3. In section 4, the verification studies conducted for the rod and the square prism are reported, and preliminary validation for the turbulent intensity in the wake of the rod is provided. In section 5, the results obtained for the ambient free stream turbulence (FST) and 3.3% and 6.8% turbulence intensity cases (named as T0, T1 and T2) are reported along with equivalent experimental data for throughout validation. Drag coefficient, base pressure coefficient, mean and fluctuating pressure coefficient distributions, time-averaged streamlines, and distributions of mean streamwise velocity and standard deviation of streamwise, and cross-stream fluctuating velocity components are considered to assess the accuracy and effectiveness of the proposed 2D URANS approach to study FST effects on bluff bodies.

2. Formulation

2.1. Computational fluid mechanics formulation

One of the key issues in this piece of research is the feasibility of applying relatively inexpensive CFD approaches to address bluff body aerodynamics problems under different levels of small-scale free stream turbulence (FST). To this end, the well stablished 2D URANS formulation has been adopted, along with the two-equation k-ω SST turbulence model (Menter and Esch, 2001), which might be considered the standard in industrial applications in wind engineering.

For incompressible flow at low Mach numbers, the Reynolds-averaged continuity and momentum equations in Cartesian coordinates are (Wilcox, 2006):

$$\frac{\partial U_i}{\partial x_i} = 0 \tag{1}$$

$$\rho \frac{\partial U_i}{\partial t} + \rho U_j \frac{\partial U_i}{\partial x_j} = \frac{-\partial P}{\partial x_j} + \frac{\partial}{\partial x_j}\left(2\mu S_{ij} - \rho \overline{u_i' u_j'}\right) \tag{2}$$

In the above equation, U_i stands for the mean speed vector, x_i represents the Cartesian coordinates, P is the mean pressure, ρ is the density of the fluid, t is the time variable, μ is the molecular viscosity of the fluid, S_{ij} represents the mean strain-rate tensor, u_i' is the fluctuating component of the flow velocity associated with turbulence that defines the so-called

Reynolds stress tensor, and the overbar ¯ stands for the time-average operator.

The specific Reynolds stress tensor term in the right hand term in equation (2), is modelled applying the Boussinesq approximation:

$$\tau_{ij} = -\overline{u_i' u_j'} = 2\nu_T S_{ij} - \frac{2}{3}k\delta_{ij}, \tag{3}$$

ν_T being the kinematic eddy viscosity, k the specific turbulent kinetic energy and δ_{ij} the unit matrix.

2.2. Triple decomposition and turbulence intensity assessment in URANS models

The flow around a bluff body presents organized flow structures such as von-Karman vortices along with random turbulent oscillations. Following Wilcox (2006) and Hussain and Reynolds (1972), any velocity component u_i might be separated into three components:

$$U_i(x,t) = \overline{U_i}(x) + u_i(x,t) = \overline{U_i}(x) + \widetilde{u_i}(x,t) + u_i'(x,t), \tag{4}$$

where $\overline{U_i}(x)$ represents the time invariant mean, and $u_i(x,t)$ is the total fluctuating component that comprises two different contributions: $\widetilde{u_i}(x,t)$ representing the organized motion, which is a zero-mean cyclical process, and $u_i'(x,t)$ that contains the random turbulent fluctuations. The URANS approach provides $U_i(x,t)$, that is the summation of the time invariant mean $\overline{U_i}(x)$ and the large scale coherent unsteady flow features $\widetilde{u_i}(x,t)$; while the turbulent oscillations $u_i'(x,t)$ are embedded in the specific Reynolds stress tensor, which is the time-averaged rate of momentum transfer due to turbulence.

The URANS simulations completed in the present study provide the time dependent flow in which the fluctuations would correspond only to the large scale coherent oscillations. Hence, as the evaluation of the turbulence intensity should include only the turbulent components yielded by the specific Reynolds stress tensor, the turbulence intensity is evaluated as:

$$It_i = \frac{\sqrt{\overline{u_i' u_i'}}}{U_\infty} = \frac{\sqrt{-\tau_{ii}}}{U_\infty} \tag{5}$$

where U_∞ is the reference mean free stream velocity and τ_{ii} represents the corresponding component of the specific Reynolds stress tensor. In the above equation, $\sqrt{\overline{u_i' u_i'}}$ is the root mean square of the turbulent fluctuations for the i-th wind flow component.

2.3. Fundamental aerodynamic parameters

The assessment of the feasibility of the proposed 2D URANS approach to correctly reproduce the aerodynamic response of bluff bodies under different levels of FST relies on the comparison of fundamental aerodynamic parameters with equivalent experimental results in the literature. These aerodynamic parameters are defined as follows.

The force coefficients represent the non-dimensional aerodynamic force components per unit of span length acting on the body under study. Sub-indexes d, l and m stand for the drag, lift and moment components. They are evaluated as:

$$C_d = \frac{F_d}{\frac{1}{2}\rho U_\infty^2 D}, C_l = \frac{F_l}{\frac{1}{2}\rho U_\infty^2 D}, C_m = \frac{M}{\frac{1}{2}\rho U_\infty^2 D^2}, \tag{6}$$

where F_d represents the drag force per unit of span length, F_l is the lift force per unit of span length and M is the centroid-axis moment per unit of span length (sign conventions are provided in Fig. 1). Additionally, in equation (6), D is the reference dimension of the body under study, which is the side of the square prism D_S in the application case considered herein.

The Strouhal number, which is a non-dimensional parameter related with the frequency of the periodic aerodynamic excitation due to vortex shedding, is defined as:

$$St = \frac{fD}{U_\infty}, \tag{7}$$

being f the dominant frequency in the lift force spectrum.

The mean pressure coefficient and the standard deviation of the pressure coefficient at any location over the surface of the body are evaluated as follows, where p is the time-dependent pressure at the considered location, and the symbol $\sim$ represents the standard deviation and ¯ the time-averaged operation:

$$\overline{C_p} = \frac{\overline{p}}{\frac{1}{2}\rho U_\infty^2}, \widetilde{C_p} = \frac{\widetilde{p}}{\frac{1}{2}\rho U_\infty^2}. \tag{8}$$

The base pressure coefficient is evaluated considering the mean pressure distribution over the complete leeward face of the square prism. The formulation is the following:

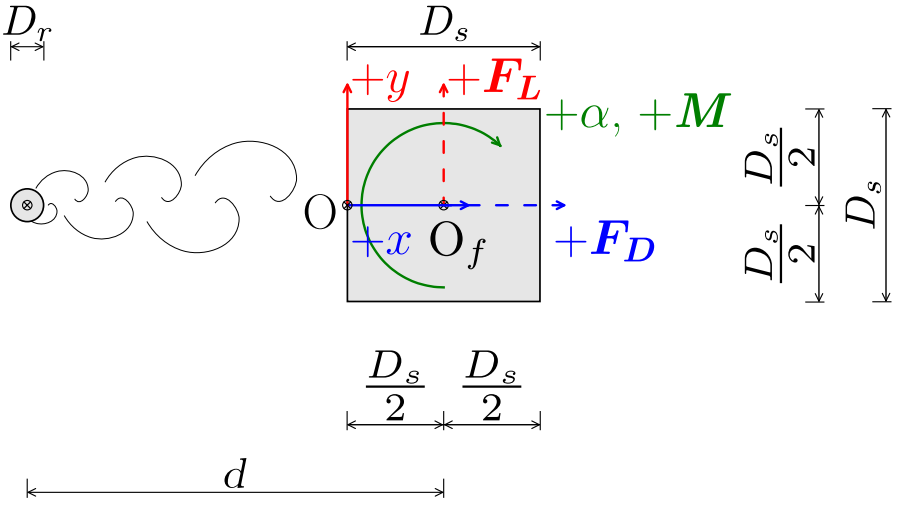

Fig. 1. Sign convention (D_s stands for the square cylinder side length and D_r for the rod diameter, O is the origin for the distances and O_f is the centroid of the square that is the reference point for the forces and moments, and d is the distance between the centers of the upstream rod and the square prism).

$$C_{pb} = \frac{\oint\oint \bar{p} dA_l}{\frac{1}{2}\rho U_\infty^2 A_l}, \tag{9}$$

where A_l represents the area of the leeward side of the body.

2.4. CFD verification metrics

In accordance with Oberkampf and Roy (2010), one of the key factors required to rigorously assess the accuracy of a CFD simulation, and therefore bring credibility to the presented computational results, is providing the uncertainty levels for the quantities of interest. Hence, a verification metric is used in order to obtain these uncertainties. Furthermore, the mesh selection for final results should be based on both a reduced level of uncertainty and a reasonable computational cost. Spatial discretization is the main source of uncertainty in CFD applications (Eça & Hoekstra, 2014), and in this paper, this is assessed by means of the method proposed by Celik et al. (2008). This proposed method reports the following parameters: the observed order of grid convergence g_c, the approximate relative error e_a, the extrapolated relative error e_{ext} and the grid convergence index for the fine mesh GCI_{fine}. Detailed description of the formulation is presented in appendix A. The same method is also applied in this paper to assess the impact on the results of the temporal discretization adopted.

3. Computational modeling

3.1. Problem description

The application of 2D URANS to address the complex aerodynamic response of a bluff body under different FST levels implies a drastic simplification in the physics of the problem, as it is three-dimensional in nature and involves phenomena such as turbulent transition, far beyond the reach of two-equation turbulence models. Therefore, the computational approach adopted herein requires a careful validation using experimental data in the literature in order to assess its merit. The focus of the validation is placed not only in the stark comparison of numerical results and experimental values, but also in the level of qualitative agreement and the potential usefulness for industrial applications.

In the introduction, the fundamentals of rod-generated small-scale turbulence have been explained. Here the same arrangement as in Gartshore (1973) is adopted for the 2D URANS simulations that are reported next. The level of turbulence in the flow reaching the body placed in the wake of the rod depends on the distance between the rod and the windward face of the body as the random fluctuations slowly dissipate downstream. The longer the distance, the lower the turbulence intensity in the flow impinging the windward face of the body. In order to soundly validate the computational outputs, the results are compared with available data in the previous reference as well as presented by Lander et al. (2016) for 1% (ambient turbulence) and 6.5% (enhanced turbulence) FST levels.

In Fig. 1, a sketch of the arrangement was provided and the reference coordinate system was also depicted. In this paper, the low FST case is referred to as case T0. This case presents no rod upstream of the prism and the nominal turbulent intensity at the inlet was set to 1%. Case T1 represents a medium FST level, with the rod placed at an upwind distance d from the centerline of the square prism $d/D_r = 212.37$. Similarly, for the T2 case, representing an enhanced FST level, the distance between the centers of the rod and the prism is $d/D_r = 56.59$. The concrete levels of turbulence intensity for cases T0, T1 and T2 are provided in a latter section. The numerical results reported in the forthcoming sections have not been corrected due to blockage effects because of the large dimensions adopted for the computational flow domain.

3.2. Computational approach

A sketch of the overall fluid domain for the 2D simulations comprising the square prism and the upstream rod is depicted in Fig. 2a, and the main dimensions are presented in Table 1. For the spatial discretization of the fluid domain, a non-conformal structured quadrangular mesh has been adopted. The fluid domain has been subdivided in 5 different zones, and the representation of these zones is provided in Fig. 2b. It is to note that in Zone 1, the boundary layer grids around the rod and/or the square prism are included, along with wake region refinements, containing conformal elements with different cell sizes. The number of elements in the boundaries separating the different zones decreases by a ratio of 2 as the number in the identification label increases.

At the inlet, Neumann boundary conditions were imposed for the pressure, while Dirichlet conditions were applied to the velocity, the specific dissipation rate and the turbulent kinetic energy. The turbulence kinetic energy and the specific dissipation were calculated considering an incoming turbulence intensity at the inlet of 1.0% and a length scale of $0.1D_s$. In the case of the outlet boundary, Neumann conditions have been considered for the velocity, the specific dissipation rate and the turbulent kinetic energy fields, while Dirichlet conditions were applied to the pressure. For the upper and lower boundaries of the fluid domain a slip wall boundary condition was selected. In the prism and rod walls, no penetration and no-slip boundary conditions were applied.

For the 2D URANS simulations, the CFD solver of choice has been OpenFOAM, adopting the k-ω.SST turbulence model. The advancement in time is done by applying the second order backward scheme, also called Second Order Upwind Euler (SOUE) scheme (Moukalled et al., 2016). For the surface normal gradient terms, the explicit non-orthogonal correction was adopted, while for the gradient schemes, the second order Gaussian integration has been chosen. Similarly, for the diffusive schemes, the unbounded second order scheme has been applied and for the convective terms, the linear upwind differential scheme has been used. Furthermore, the PIMPLE algorithm manages the pressure velocity coupling in the unsteady Navier Stokes equations.

In Fig. 3, details of mesh discretization, for the fine discretization level and the case in which the rod and square prism are separated for a distance $d/D_r = 56.59$ are presented. The difference in the characteristic size between the rod and the prism (Fig. 3c) as well as the large number of cells required to properly simulate the behavior of the boundary layer and shear layers of the upstream rod are noteworthy.

4. Verification and preliminary validation

The two geometries considered in this study, the rod and the square prism, have different characteristic dimensions, as the prism side length is one order of magnitude larger than the diameter of the rod ($D_s = 12\ D_r$). Consequently, the verification studies have been conducted independently for each geometry. For the FST studies that are latter reported in the Results section, comprising both the rod and the prism, the mesh characteristics in the vicinity of each geometry are based upon the verification studies presented below.

Three meshes with different levels of spatial discretization are adopted for each geometry, and the method proposed by Celik et al. (2008) introduced in section 2 has been applied, yielding the results that are reported next. Once the most adequate mesh arrangement, balancing computational demands and sensitivity with the level of spatial discretization, has been selected for each geometry, additional temporal verification studies have been conducted using three different maximum Courant numbers. The simulations for the initial spatial discretization sensitivity studies have been conducted at a maximum Courant number, $Co = 0.5$.

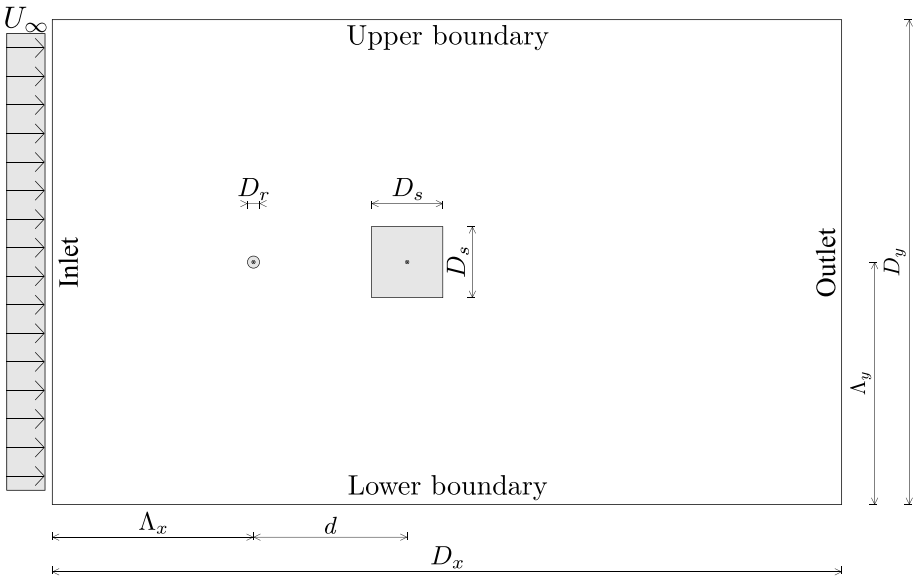

a) Overall fluid domain (not to scale).

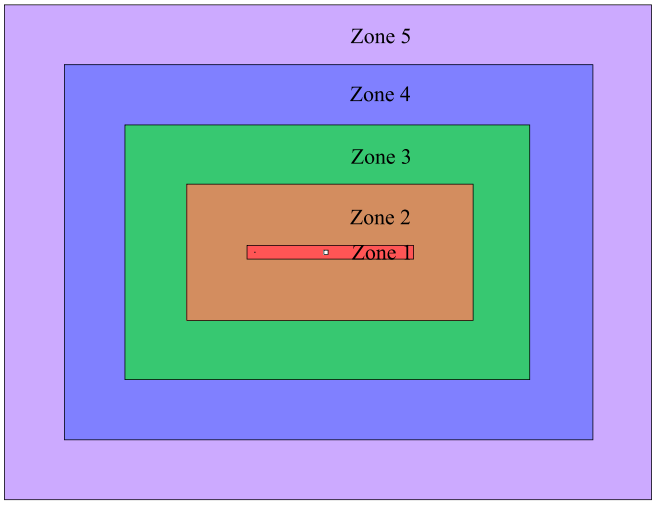

b) Different zones in which the mesh is subdivided.

Fig. 2. Fluid domain definition.

Table 1
Overall fluid domain dimensions.[a]

Λ_x	Λ_y	D_x	D_y
60 D_s	60 D_s	160.5 D_s + x	120 D_s

[a] D_s is the side of the square cylinder, Λ_x is the distance from the inlet to the centre of the rod, in case of being present, otherwise it is be the distance from the inlet to the centre of the square prism, Λ_y is the distance from the centre of the square cylinder to both the upper and lower boundaries, D_x and D_y are respectively the total width and height of the fluid domain.

All the simulations have been completed at the same Reynolds number $\mathrm{Re} = (UD_s)/\nu = 3.84 \times 10^4$, based on the prisms side D_s. This Reyonolds number is the same as in the experiments conducted by Gartshore (1973), and is also close to $\mathrm{Re} = 5.3 \times 10^4$ in Lander et al. (2016).

4.1. Spatial verification for the isolated rod

The non-dimensional cell sizes of the elements located at the external perimeter of the fluid domain are presented in Table 2 for the three refinement levels considered in the spatial verification study. The characteristics of the boundary layer of the meshes used for the spatial verification study are presented in Table 3 for the isolated rod and square prism, while in Table 4 their y^+ values can be found. It should be borne in mind that the y^+ value has been calculated considering the total height of the first element of the boundary layer.

In Table 5, the integral parameters and the Strouhal number obtained for the isolated rod are presented for the three different levels of spatial discretization. In the table, a summary of the fundamental results in the uncertainty assessment in the integral parameters associated with the mesh density is also included, providing the complete set of results in appendix B. Furthermore, due to their paramount importance in the numerical simulation of rod-induced turbulent flow, the longitudinal

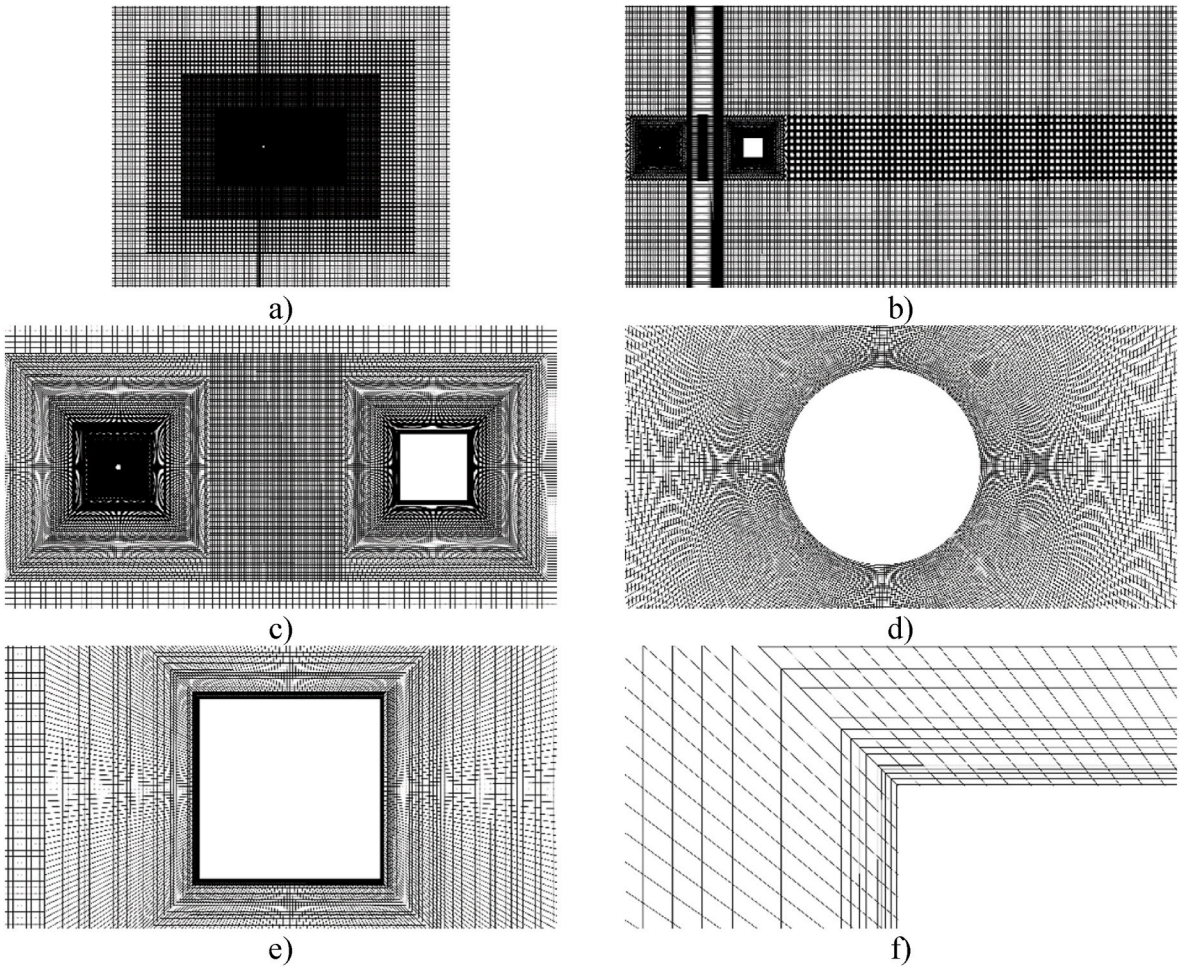

Fig. 3. Mesh details of the selected mesh for the case in which the rod and the square prism are separated a distance $d/D_r = 56.59$: a) overall fluid domain, b) detail of the wake, c) detail of the mesh around the rod and the square prism, d) boundary layer of the rod, e) detail of the mesh around the square prism and f) detail of the boundary layer of the square prism.

Table 2
Cell size of the elements at the most exterior boundary of the fluid domain. The sizes have been made non-dimensional by dividing them by D_r.

	coarse	medium	fine
Non-dimensional size at the external perimeter	20.4	13.6	8.16

turbulence intensity values along the rod wake centerline are presented in Table 6. The verification study for the rod also considers the streamwise turbulence intensity wake centerline profile, as this is a cornerstone feature in the proposed 2D URANS approach for the FST studies.

Fig. 4 represents the total fluctuating streamwise velocity component profile along the wake centerline of the isolated rod, obtained for the three different meshes considered. The chart shows how the differences between the distributions are reduced with the successive refinement of the mesh.

Based on results reported in Tables 5 and 6, the fine mesh has been selected, as the low uncertainty values obtained for the turbulence intensity and integral parameters indicate that the spatial refinement has reached convergence, and therefore no further refinement would produce a significant variation in the monitored parameters. The importance of conducting the space discretization sensitivity study is remarked, as the turbulence intensity values might show some

Table 3
Boundary layer characteristics and overall number of elements of the meshes for the rod spatial verification study.[b]

		y_1/D_r	r	n_{BL}	y_{BL}/D_r	Overall #elements
rod	coarse	6.957×10^{-3}	1.11	20	0.425	84876
	medium	7.114×10^{-3}	1.07	20	0.300	180220
	fine	7.276×10^{-3}	1.04	20	0.221	507984
Square prism	coarse	8.956×10^{-3}	1.22	20	2.120	80396
	medium	9.140×10^{-3}	1.20	20	1.564	169852
	fine	9.240×10^{-3}	1.16	20	1.075	478224

[b] y_1 is the height of the first element of the boundary layer (BL) mesh, D_i is the rod diameter or the square prism side, r is the growth ratio of the elements in the BL, n_{BL} is the number of layers forming the BL mesh and y_{BL} is the total height of the BL mesh.

Table 4
y^+ values for the meshes considered in the spatial discretization study of the isolated rod and square prism.

		$\overline{y^+}$	$\%\overline{y^+ > 2}$	$\%\overline{y^+ > 4}$	$\%\overline{y^+ > 6}$
rod	coarse	2.38	45.31	23.44	0.00
	medium	2.42	45.31	25.00	0.00
	fine	2.51	51.56	26.25	0.00
Square prism	coarse	1.25	10.94	1.56	0.00
	medium	1.30	10.42	2.08	1.04
	fine	1.21	10.00	1.88	0.63

differences with mesh refinement levels. High spatial discretization sensitivity was identified at $d/D_r = 44.94$, as the turbulence intensity changed from 4.7% (coarse mesh), to 6.3% (medium mesh), reaching finally 7.2% (fine mesh).

For the rod, the time-averaged drag coefficient of 1.5 (Table 5) is larger than the value of about 1.1 for circular cylinders in the subcritical range; however, this is due to the two-dimensional approach adopted. In Cao and Tamura (2015), 3D LES simulations with different aspect ratios show higher values for the mean drag coefficient and the standard deviation of the lift coefficient as the aspect ratio decreases, due to the inability to properly simulate the three-dimensional features of the flow. For an aspect ratio of 1, Cao and Tamura (2015) reported a drag coefficient slightly above 1.5 and a standard deviation of the lift coefficient just below 1, in alignment with our results in Table 5 for the fine mesh case.

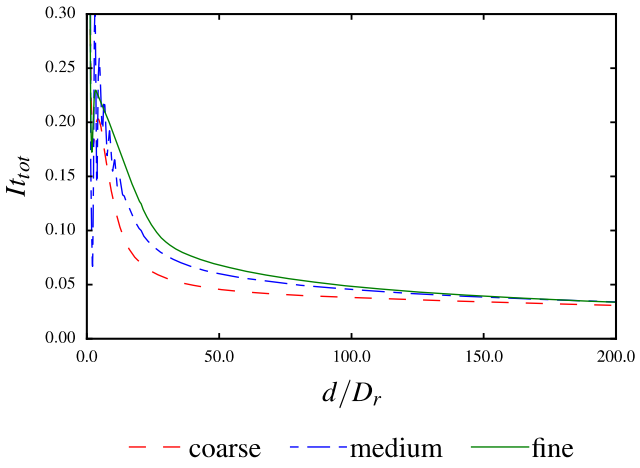

Fig. 4. Total fluctuating streamwise velocity component profile along the wake centerline of the isolated rod for the three different meshes considered in the verification study.

Moreover, in Fig. 5a the wake centerline profile for the streamwise fluctuating velocity components obtained for the fine mesh is compared with wind tunnel data in Gartshore (1973) and Tang et al. (2016) for preliminary validation. The ability of 2D URANS simulations to

Table 5
Spatial sensitivity study of the rod.[c] (See appendix B for the complete set of data of the verification study.).

	$\overline{C_d}$	$\overline{C_l}$	$\overline{C_m}$	$\tilde{C_d}$	$\tilde{C_l}$	$\tilde{C_m}$	St
coarse (3)	1.480	−0.001	0.000	0.099	1.012	0.002	0.236
medium (2)	1.514	0.030	0.000	0.129	1.141	0.003	0.199
fine (1)	1.503	0.003	0.000	0.104	1.018	0.002	0.202
g_c	4.35	0.50	0.02	0.72	0.17	0.48	10.13
e_a^{21}	0.007	8.101	0.024	0.234	0.121	0.345	0.014
e_{ext}^{21}	0.002	1.024	1.000	4.843	2.055	2.091	0.0004
GCI_{fine}^{21}	0.002	54.091	4.05×10^4	1.036	2.435	2.396	0.0005
$\pm U_{fine}^{21} \times 10^3$	3.678	177.74	80.398	108.14	2479.9	4.895	0.109

[c] The numbers between parenthesis are the subindexes referring to the discretization level in the verification process. g_c is the apparent order of convergence, e_a^{21} is the approximate relative error between the fine and medium mesh, e_{ext}^{21} is the extrapolated relative error between the fine and medium mesh, GCI_{fine}^{21} is the grid convergence index of fine mesh, and U_{fine}^{21} is the uncertainty associated with the fine mesh.

Table 6
Spatial sensitivity study of the rod for the longitudinal turbulence intensity at different distances from the center of the rod (d/D_r).[d] (See appendix B for the complete set of data of the verification study.).

	It_u								
d/D_r	44.94	68.80	79.72	92.67	116.28	119.58	140.39	159.69	164.77
coarse (3)	0.047	0.042	0.040	0.039	0.037	0.036	0.035	0.033	0.033
medium (2)	0.063	0.053	0.050	0.047	0.043	0.042	0.040	0.037	0.037
fine (1)	0.072	0.058	0.054	0.050	0.045	0.044	0.041	0.038	0.037
g_c	3.02	3.56	3.50	4.18	4.96	5.09	6.27	8.11	8.75
e_a^{21}	0.123	0.094	0.087	0.067	0.045	0.043	0.027	0.015	0.012
e_{ext}^{21}	0.063	0.037	0.035	0.020	0.010	0.008	0.003	0.001	0.001
GCI_{fine}^{21}	0.084	0.049	0.046	0.026	0.013	0.011	0.004	0.001	0.001
$\pm U_{fine}^{21} \times 10^3$	5.999	2.841	2.498	1.313	0.561	0.494	0.177	0.046	0.029

[d] The numbers between parenthesis are the subindexes referring to the discretization level in the verification process. g_c is the apparent order of convergence, e_a^{21} is the approximate relative error between the fine and medium mesh, e_{ext}^{21} is the extrapolated relative error between the fine and medium mesh, GCI_{fine}^{21} is the grid convergence index of fine mesh, and U_{fine}^{21} is the uncertainty associated with the fine mesh.

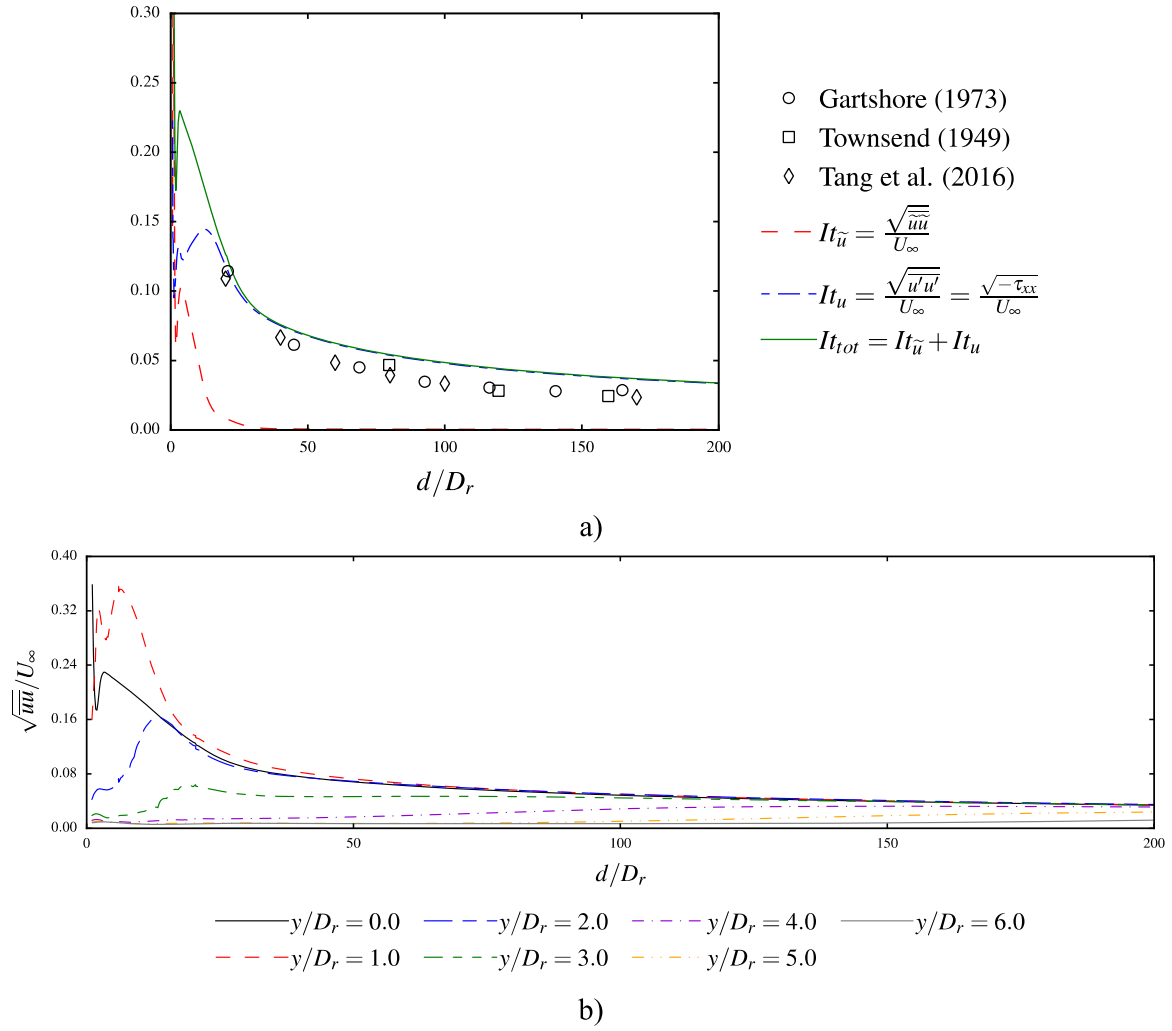

Fig. 5. Streamwise turbulence profile in the wake of the isolated rod for the selected mesh (fine mesh), considering the different contributions to its total value.

meaningfully reproduce the variation of FST intensity depending on the downstream distance from the rod is paramount within the scope of this research. In the figure, the contribution of the random velocity oscillations (dashed blue line) is provided along with the coherent fluctuations (dashed red line) and the total fluctuating component (continuous green line). The presence of the fluctuating coherent component due to the vortices shed from the rod is apparent only for a distance up to $d/D_r \cong 35$, as the vortical structures dissipate as they drift away from the rod. In this manner, only the turbulent fluctuations remain farther downstream in the wake of the rod. For the cases considered in this study, the distances between the rod and the bluff body are in the range where the coherent oscillations in the velocity might be considered as negligible, so the impinging flow on the bluff body may be considered representative of a free stream small scale turbulent flow. The comparison of the turbulence intensity along the rod wake centerline and the experimental data in Gartshore (1973), Townsend (1949) and Tang et al. (2016) is good, even at large distances from the rod. In Fig. 5b, the longitudinal profiles in the range y/D_r=0 to 6 are provided to show the variation in the turbulence intensity over the square depth. It is to note that according to Gartshore (1973) the turbulence at the upstream stagnation line of the bluff body *"is effective in modifying its flow pattern"*.

4.2. Spatial verification for the isolated square prism

In Table 7, the results obtained for the integral parameters and Strouhal number of the isolated square prism are presented. Similarly to the rod case, the simulations have been conducted at a maximum Courant number $Co = 0.5$.

As for the case of the rod, the selected mesh for the square prism is the fine one. It is noteworthy that the Strouhal number provided by the fine mesh is lower than the experimental values for the square prism, between 0.12 and 0.13 (Zhao et al., 2021). According to our spatial density sensitivity study, a higher density mesh slightly decreases the frequency of vortex shedding, as can be inferred from Table 7. Furthermore, the grid typology might impact the values obtained for the integral parameters, and the type of turbulence model, the choice of the values of model parameters, and the selection of the discretization schemes, also influence the numerical outputs (Bruno and Khris, 2003; Bruno and Oberto, 2022).

Table 7
Spatial sensitivity study of the prism.[e] (See appendix B for the complete set of data of the verification study.).

	$\overline{C_d}$	$\overline{C_l}$	$\overline{C_m}$	$\tilde{C_d}$	$\tilde{C_l}$	$\tilde{C_m}$	St
coarse (3)	2.183	0.060	0.013	0.166	1.504	0.114	0.132
medium (2)	2.191	−0.087	−0.015	0.210	1.558	0.118	0.112
fine (1)	2.169	−0.003	−0.001	0.250	1.617	0.122	0.109
g_c	2.60	1.97	2.39	1.50	0.84	1.31	8.23
e_a^{21}	0.010	25.468	0.263	0.159	0.036	0.032	0.025
e_{ext}^{21}	0.007	1.040	1.051	0.190	0.098	0.054	0.002
GCI_{fine}^{21}	0.009	32.552	25.690	0.294	0.135	0.071	0.002
$\pm\, U_{fine}^{21} \times\ 10^3$	18.631	107.16	14.000	73.535	21.908	8.678	0.213

[e] The numbers between parenthesis are the subindexes referring to the discretization level in the verification process. g_c is the apparent order of convergence, e_a^{21} is the approximate relative error between the fine and medium mesh, e_{ext}^{21} is the extrapolated relative error between the fine and medium mesh, GCI_{fine}^{21} is the grid convergence index of fine mesh, and U_{fine}^{21} is the uncertainty associated with the fine mesh.

4.3. Temporal verification

For the temporal discretization sensitivity study, which has been conducted for the fine mesh selected in the previous section, three different maximum Courant numbers have been considered, $Co = 0.5$, 1.0 and 2.0. In Tables 8–10, the results of the temporal verification study conducted applying the method proposed by Celik, are presented for the isolated rod, considering the integral parameters and the wake centerline streamwise turbulence intensity profile, along with the isolated square prism, to assess the uncertainty in the integral parameters. The

Table 8
Temporal sensitivity study of the rod for the integral parameters and Strouhal number.[f] (See appendix B for the complete set of data of the verification study.).

	$\overline{C_d}$	$\overline{C_l}$	$\overline{C_m}$	$\tilde{C_d}$	$\tilde{C_l}$	$\tilde{C_m}$	St
large (3)	1.438	0.001	0.000	0.079	0.972	0.002	0.180
regular (2)	1.487	0.003	0.000	0.096	1.009	0.002	0.195
short (1)	1.503	0.003	0.000	0.104	1.018	0.002	0.202
g_c	1.57	1.66	1.00	1.01	1.97	0.24	1.01
e_a^{21}	0.011	0.173	1.000	0.080	0.009	0.049	0.036
e_{ext}^{21}	0.005	0.074	0.500	0.073	0.003	0.384	0.035
GCI_{fine}^{21}	0.007	0.100	1.250	0.099	0.004	0.347	0.045
$\pm\, U_{fine}^{21} \times\ 10^3$	10.362	0.330	0.003	10.287	4.045	0.708	0.009

[f] The numbers between parenthesis are the subindexes referring to the discretization level in the verification process. g_c is the apparent order of convergence, e_a^{21} is the approximate relative error between the fine and medium mesh, e_{ext}^{21} is the extrapolated relative error between the fine and medium mesh, GCI_{fine}^{21} is the grid convergence index of fine mesh, and U_{fine}^{21} is the uncertainty associated with the fine mesh.

Table 10
Temporal sensitivity study of the prism.[h] (See appendix B for the complete set of data of the verification study.).

	$\overline{C_d}$	$\overline{C_l}$	$\overline{C_m}$	$\tilde{C_d}$	$\tilde{C_l}$	$\tilde{C_m}$	St
large (3)	2.129	−0.005	−0.001	0.247	1.605	0.119	0.105
regular (2)	2.149	0.036	0.007	0.245	1.613	0.121	0.107
short (1)	2.169	−0.003	−0.001	0.250	1.617	0.122	0.109
g_c	0.03	0.07	0.08	1.15	0.95	0.67	0.50
e_a^{21}	0.009	12.041	14.349	0.022	0.003	0.010	0.014
e_{ext}^{21}	0.284	0.996	0.996	0.018	0.003	0.016	0.033
GCI_{fine}^{21}	0.496	315.65	320.22	0.022	0.003	0.020	0.042
$\pm U_{fine}^{21} \times 10^3$	1076.0	1039.1	174.52	5.603	5.570	2.444	4.606

[h] The numbers between parenthesis are the subindexes referring to the discretization level in the verification process. g_c is the apparent order of convergence, e_a^{21} is the approximate relative error between the fine and medium mesh, e_{ext}^{21} is the extrapolated relative error between the fine and medium mesh, GCI_{fine}^{21} is the grid convergence index of fine mesh, and U_{fine}^{21} is the uncertainty associated with the fine mesh.

Table 9
Temporal sensitivity study of the rod for the longitudinal turbulence intensity at different distances from the center of the rod (x/D_s).[g] (See appendix B for the complete set of data of the verification study.).

	It_u								
$d/\ D_r$	44.94	68.80	79.72	92.67	116.28	119.58	140.39	159.69	164.77
large (3)	0.075	0.060	0.056	0.052	0.046	0.046	0.042	0.039	0.039
regular (2)	0.072	0.059	0.055	0.051	0.045	0.045	0.041	0.038	0.038
short (1)	0.072	0.058	0.054	0.050	0.045	0.044	0.041	0.038	0.037
g_c	1.82	1.15	1.06	1.14	1.08	1.07	1.20	1.58	1.15
e_a^{21}	0.010	0.010	0.011	0.010	0.011	0.011	0.010	0.008	0.011
e_{ext}^{21}	0.004	0.008	0.010	0.009	0.010	0.010	0.008	0.004	0.008
GCI_{fine}^{21}	0.005	0.010	0.012	0.011	0.012	0.013	0.010	0.005	0.011
$\pm\, U_{fine}^{21} \times\ 10^3$	0.338	0.609	0.678	0.536	0.552	0.563	0.416	0.201	0.416

[g] The numbers between parentheses are the subindexes referring to the discretization level in the verification process. g_c is the apparent order of convergence, e_a^{21} is the approximate relative error between the fine and medium mesh, e_{ext}^{21} is the extrapolated relative error between the fine and medium mesh, GCI_{fine}^{21} is the grid convergence index of fine mesh, and U_{fine}^{21} is the uncertainty associated with the fine mesh.

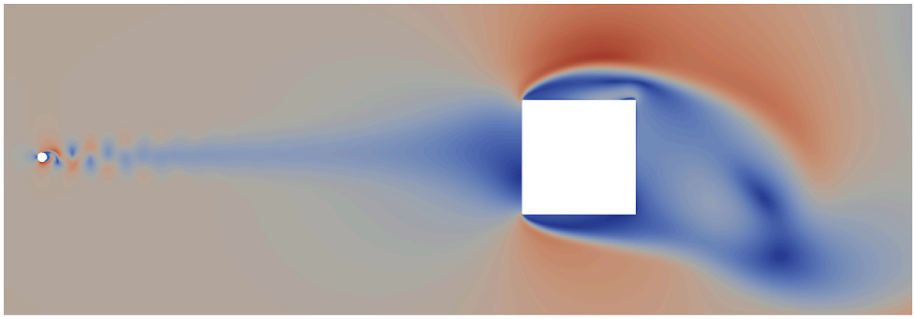

Fig. 6. Velocity magnitude snapshot for the case T2.

full set of results for the verification studies are presented in appendix B.

For the temporal discretization at $Co = 0.5$, the uncertainty values obtained for the different parameters under study are acceptable, and further decrement in the time step would only increment the computational cost without adding a substantial improvement in the accuracy of the results. It is noteworthy that the very low uncertainty obtained for the turbulence intensity values in the wake of the rod, which is the most important parameter in this study, suggests that these values are almost insensitive to the time step for the selected mesh.

5. Results

In this section the results obtained by applying the proposed 2D URANS approach are presented and discussed. Three different turbulence intensity levels are considered depending on the presence of the upstream rod and the distance between the rod and the downwind square prism. The nominal turbulence intensities at the location of the square prism are: 0.7% (ambient turbulence resulting from the decay of the 1% turbulence intensity prescribed at the inlet, with the upstream rod absent, and case referred to as T0), 3.3% (distance between the rod and square 212.37 D_r, referred to as T1) and 6.8% (distance between the rod and the square 56.59 D_r, referred to as T2). The assessment of the accuracy of the numerical simulations is based on the direct comparison with equivalent experimental data in the literature. The reference wind tunnel measurements for rod-induced turbulent flow are the results reported in Gartshore (1973) and Lander et al. (2016) for ambient conditions (1% and 0.6% turbulence intensity) and the so-called enhanced FST (6.5%) in Lander et al. (2016), along with the data in Gartshore (1973) for the 6.8% case. In Fig. 6, one snapshot of the velocity magnitude field for the T2 case is provided, depicting the flow structures in the wake of the rod.

5.1. Force coefficients and base pressure coefficient

A first glimpse to the predictive capabilities of the 2D URANS approach is provided by the integral parameters and their comparison with the available experimental data in the literature. Table 11 presents relevant mean and fluctuating force coefficients along with base pressure coefficients. It is noted that in Lander et al. (2016), the normalizing length adopted for the evaluation of force and base pressure coefficients

Table 11
Mean and fluctuating force coefficients, and base pressure for different FST levels. Current numerical results and equivalent experimental data in the literature.

Case	It_u[%]	$\overline{C_d}$	$\widetilde{C_d}$	$\widetilde{C_l}$	C_{pb}
T0	0.7	2.17	0.25	1.62	−1.40
Case A (Lander et al., 2016)	1.0	2.35	0.22	1.14	−1.51
Gartshore (1973)	0.6	2.22	–	–	−1.44
T1	3.3	1.93	0.12	1.41	−1.24
Gartshore (1973)	3.3	1.84	–	–	−1.20
T2	6.8	1.63	0.06	1.10	−1.05
Case B (Lander et al., 2016)	6.5	1.86	0.15	1.10	−1.22
Gartshore (1973)	6.8	1.68	–	–	−1.05

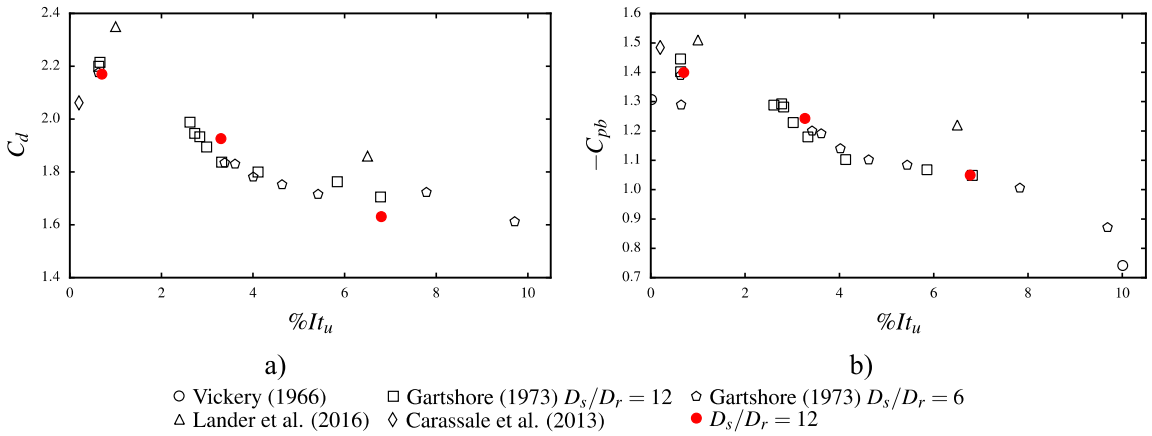

Fig. 7. Comparison between 2D URANS and experimental results for rod-induced FST acting on a square prism a) drag coefficient and b) base pressure.

is the distance between the outer most pressure locations (0.84 D_s).

For the ambient FST case, the agreement between the T0 case simulation and the values reported in Gartshore (1973) for the drag coefficient and the base pressure coefficient is very good. The comparison with the data reported in Lander et al. (2016) shows larger differences, although within the ranges expected given the higher FST level and Reynolds number in their work, as well as the inherent scattering in experimental data. Furthermore, for the higher FST levels (cases T1 and T2), the agreement with the experimental data reported in Gartshore (1973) is again good for the drag coefficient and the base pressure coefficient, while the agreement with the results in Lander et al. (2016) for T2 is reasonable, taking into account the differences in the turbulence intensity and Reynolds number previously noted. The 2D URANS approach seems capable of capturing the decrease in the mean drag coefficient and the base pressure coefficient as the FST level is increased. In Fig. 7, the numerical values obtained for the drag coefficient and the base pressure are reported along with relevant experimental data in the literature. The comparisons presented in Fig. 7 show the accuracy provided by the numerical simulations, and their remarkable ability to correctly predict the variations in the studied parameters as a function of the turbulent intensity level.

5.2. Pressure coefficient distributions

In Fig. 8, the mean and fluctuating pressure coefficients around the square prism are depicted along with experimental data for validation. It should be borne in mind the existence of certain scattering in the pressure coefficient distributions obtained experimentally around bluff bodies by different authors, as it has been documented for instance in Bruno et al. (2014). For the geometry studied at different FST levels, the agreement in the mean pressure coefficient distribution between the present simulations and the experimental data is very good along the windward face of the prism, as shown in Fig. 8a). In fact, the momentum deficit caused by the upwind rod for the 6.8% FST case coincides with the data in Lander et al. (2016) for the 6.5% FST. Over the upper and lower side faces of the square cylinder, the experimental data do not show relevant differences in the mean pressure distributions for different values of FST, and only in the proximity of the leeward corner the mean C_p decreases for the 6.5% turbulence intensity. The CFD data show lower suctions as the nominal turbulence in the flow increases, which are smaller than the wind tunnel data. On the leeward face, the experimental data show lower suctions for higher FST values. The numerical simulations show the same trend with FST on the leeward face, although the mean suctions are smaller than the ones obtained for similar FST levels in the experimental references. It is noted that in Fig. 7, the values reported in Lander et al. (2016) for the drag coefficient C_d and the base pressure coefficient C_{pb} were consistently above the trend exhibited in the results reported in Gartshore (1973), Vickery (1966) or Carassale et al. (2013), which is consistent with the higher suctions over the leeward side mentioned above.

The distribution of the standard deviation of the pressure coefficients, as shown in Fig. 8b), shows a good agreement for the considered levels of FST between the numerical simulations and the wind tunnel tests for both the windward and the leeward faces. In fact, the agreement along the leeward side is good, providing the CFD data slightly lower values than in Lander et al. (2016). The fluctuation in the pressure is mainly due to the vortex shedding process, which poses a challenge for 2D CFD simulations adopting two-equation turbulence models (Alvarez et al., 2018). For the upper and lower side faces, the agreement of the numerical simulation at 6.8% FST level with the experimental data corresponding with a FST value of 6.5% in Lander et al. (2016) is also good. In Lander et al. (2016), the fluctuation pressure coefficients along the upper and lower sides of the prism are very close for the 1% and 6.5% turbulence levels. Nevertheless, the CFD simulations provide higher distributions of fluctuating pressure coefficients, which is consistent with the higher standard deviation of the lift coefficient in Table 11.

5.3. Time-averaged flow features

The time-averaged streamlines offer a valuable qualitative description of the mean flow features around the square cylinder at different FST levels. In Fig. 9, the streamlines for cases T0, T1 and T2 show the effect caused by the turbulent content in the incoming flow as the size (height) of the recirculation region attached to the upper and lower side faces of the prism decreases with enhanced levels of FST, therefore the streamlines are closer to both the upper and lower surfaces of the square prism (see Fig. 9), which facilitates flow reattachment towards the

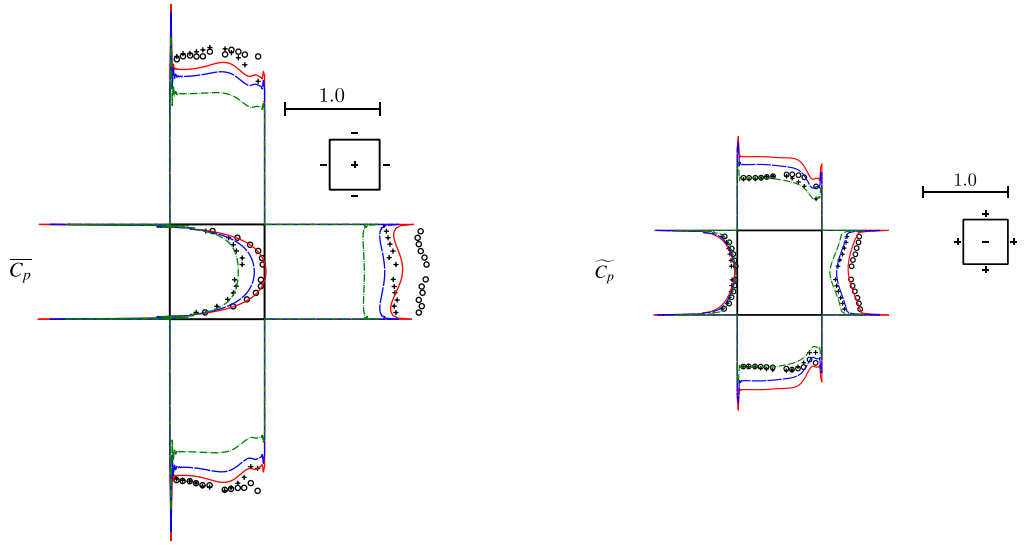

Fig. 8. a) Mean and b) fluctuating pressure coefficient distributions around the square prism for different FST levels. Numerical and experimental results.

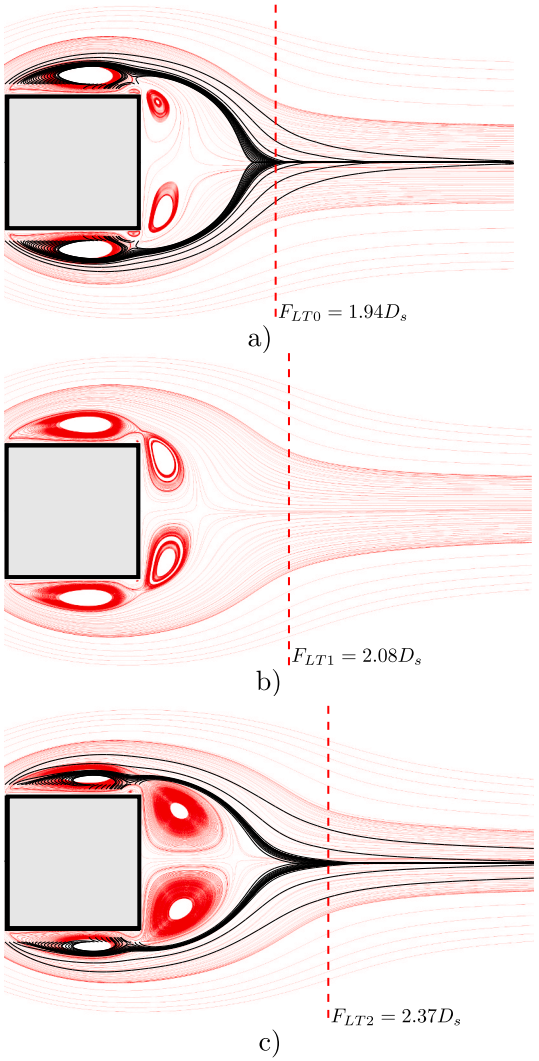

Fig. 9. Time-averaged streamlines for a) case T0, b) case T1 and c) case T2 (red), compared with the experimental values in Lander et al. (2016) (black) for 1% and 6.5% FST levels. Values of the wake formation length for the numerical simulations are provided for reference.

leeward edge. This effect is caused by the increase in the curvature of the separated shear layer (Gartshore, 1973; Lander et al., 2016). Furthermore, the time-averaged vortices in the proximity of the leeward face increase their size as higher levels of incoming turbulent flow provoke the attachment of the shear layers in the vicinity of the leeward corners and the subsequent straightening of the streamlines in the base region (the wake region from the leeward face up to the wake formation length). In the simulations, it has been observed that increased levels of FST enhance the reattachment of the shear layer in the vicinity of the leeward corner. This effect is closely linked with the decrease in the magnitude of the base pressure previously reported, as the vortices with higher negative pressure at their centers are located further downstream as the turbulence levels increase. The behavior provided by these numerical simulations is in agreement with the qualitative description in Gartshore (1973) and the PIV-based results in Lander et al. (2016). The experimental streamlines reported in Lander et al. (2016) for ambient and enhanced FST levels are presented in Fig. 9a) and c) for reference. In Fig. 9, for the numerical simulations, the wake formation length, defined as the distance along the wake centerline from the windward face to the location of the maximum cross-stream fluctuating velocity component, is also provided for reference.

5.4. Flow characteristics in the shear layer, base and wake regions

The feasibility of the proposed approach to correctly simulate the flow behavior in the most relevant regions, such as at close proximity to the afterbody, is further assessed by examining the vertical profiles of the streamwise mean velocity, fluctuating velocity components and Reynolds shear stress along the wake of the square prism. In Fig. 10, at $x/D_s = 1.5$, 2.5 and 3.5 locations (see Fig. 1), vertical profiles of streamwise mean velocity magnitude as well as standard deviations of the fluctuating streamwise and cross-stream velocity components are presented along with the equivalent experimental values in Lander et al. (2016) for validation. Furthermore, the global Reynolds shear stresses are also presented along with the available equivalent experimental values in Li et al. (2022). The agreement in the mean streamwise velocity is good, particularly for the cross-stream profiles closer to the prism. In general, the 2D approach provides higher mean streamwise velocities close to the wake centerline, while further away the mean velocity is lower than the experimental values. For the standard deviation of the streamwise and across-stream velocity components, the agreement is reasonable, at least for the cross-stream profiles located at $x/D_s = 1.5$ and 2.5. In general, the proposed approach provides shapes for the profiles similar to the experimental ones but depicting higher fluctuations in the velocity, which is consistent with the implicit perfect spanwise correlation of 2D models and strong vortical structures featured in 2D URANS, as they produce single mode large scale unsteady structures without resolving any of the details of turbulence (Menter, 2009). For the Reynolds shear stresses cross-stream profiles, the numerical results are compared with the experimental data in Li et al. (2022), which were obtained considering grid-generated FST for a $Re_D = 2.1 \times 10^4$, finding reasonable agreement, both in the shape of the profile and the magnitudes. Taking into consideration the inherent limitations in the proposed approach, its ability to simulate the very complex flow features at different rod-induced FST levels seems adequate.

Additional insights in the FST-related aerodynamics are obtained by analyzing the centerline wake profiles of mean and fluctuating velocity components. In Fig. 11, these profiles are compared with the experimental ones provided by Lander et al. (2016) and (Lyn et al., 1995). In Fig. 11a), in the region close to the leeward side of the square prism, up to $x/D_s \approx 2.0$, case T2 matches accurately the case B values in Lander et al. (2016); however, cases T0 and T1 show higher values of the mean streamwise velocity, surely due to the very energetic vortical structures in the wake of these 2D URANS models. For larger distances from the prism, the mean velocity along the wake center line for case T2 surpasses the values of case T0, in agreement with the qualitative behavior reported in Lander et al. (2016). Case T1, shows the highest mean streamwise velocity component for $x/D_s > 2.0$. For the fluctuating streamwise component profile along the wake centerline, the 2D URANS simulations offer results in qualitative agreement with experimental data in Lander et al. (2016), although the values are generally higher, except for case T2 that closely approaches the experimental values for $x/D_s > 2.5$. Furthermore, the location of the maximum value of the standard deviation of the normalized cross-stream velocity component facilitates the identification of the vortex formation length for the three different levels of FST considered herein, and this is a relevant result within the scope of this investigation. The qualitative agreement in the cross-stream velocity fluctuating component, shown in Fig. 11c), is reasonable, particularly for $x/D_s > 2.5$, with smaller fluctuations for the higher levels of FST. Furthermore, the agreement in the formation length is quite good, as the $L_F = 1.94\ D_s$ value obtained for the T0 case agrees quite well with $L_F = 2.21\ D_s$ for case A in Lander et al. (2016), which represents a 12% difference, and accounts for the slightly shorter length of the mean wake vortices in Fig. 9a), when compared with the PIV data. For T2 (6.8% FST), the formation length $L_F = 2.37\ D_s$ agrees remarkably well with $L_F = 2.46\ D_s$ reported in Lander et al. (2016). For the intermediate FST case, T1, the formation length is $L_F = 2.08\ D_s$,

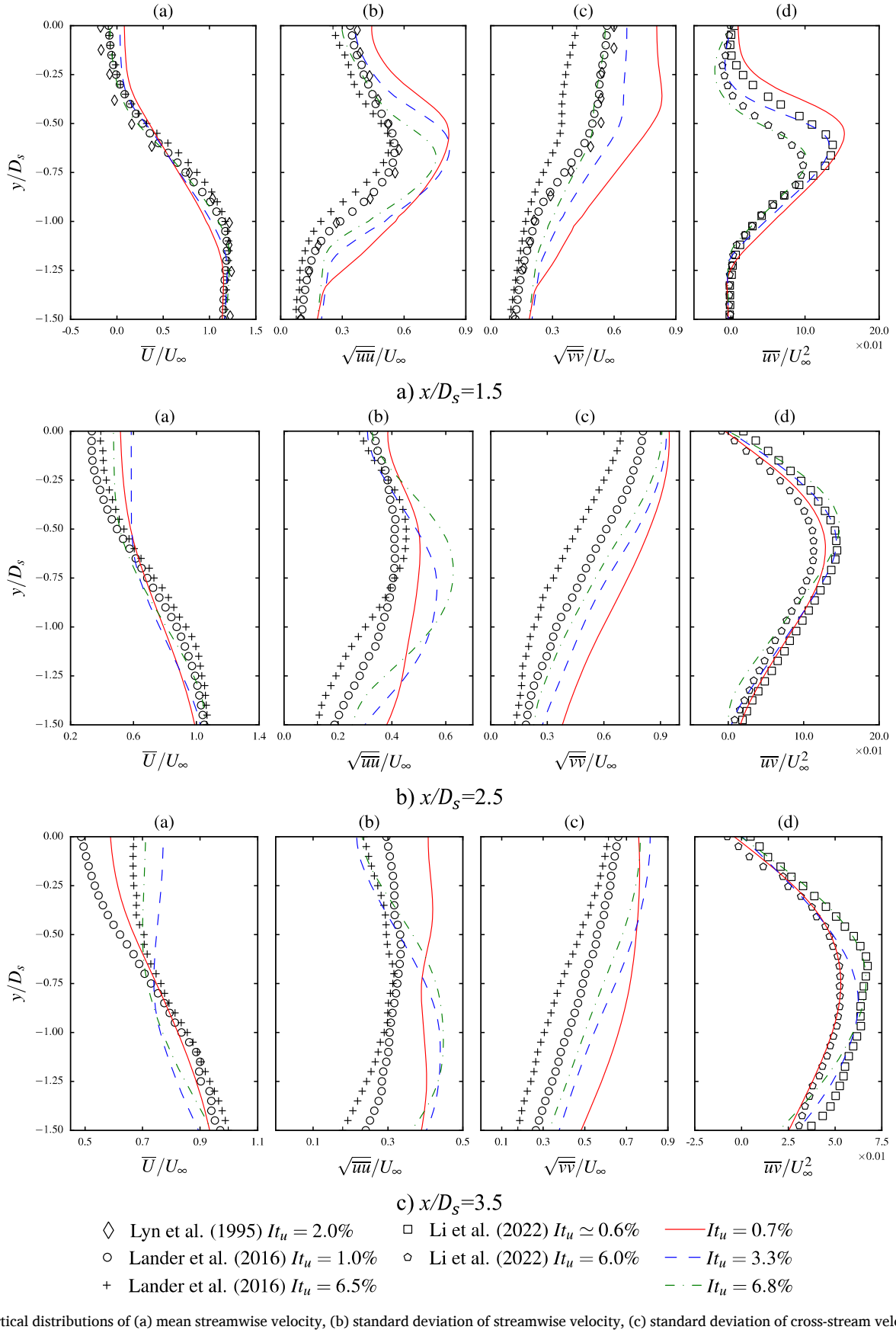

Fig. 10. Vertical distributions of (a) mean streamwise velocity, (b) standard deviation of streamwise velocity, (c) standard deviation of cross-stream velocity and (d) Reynolds shear stress components at different distances in the wake of the square prism.

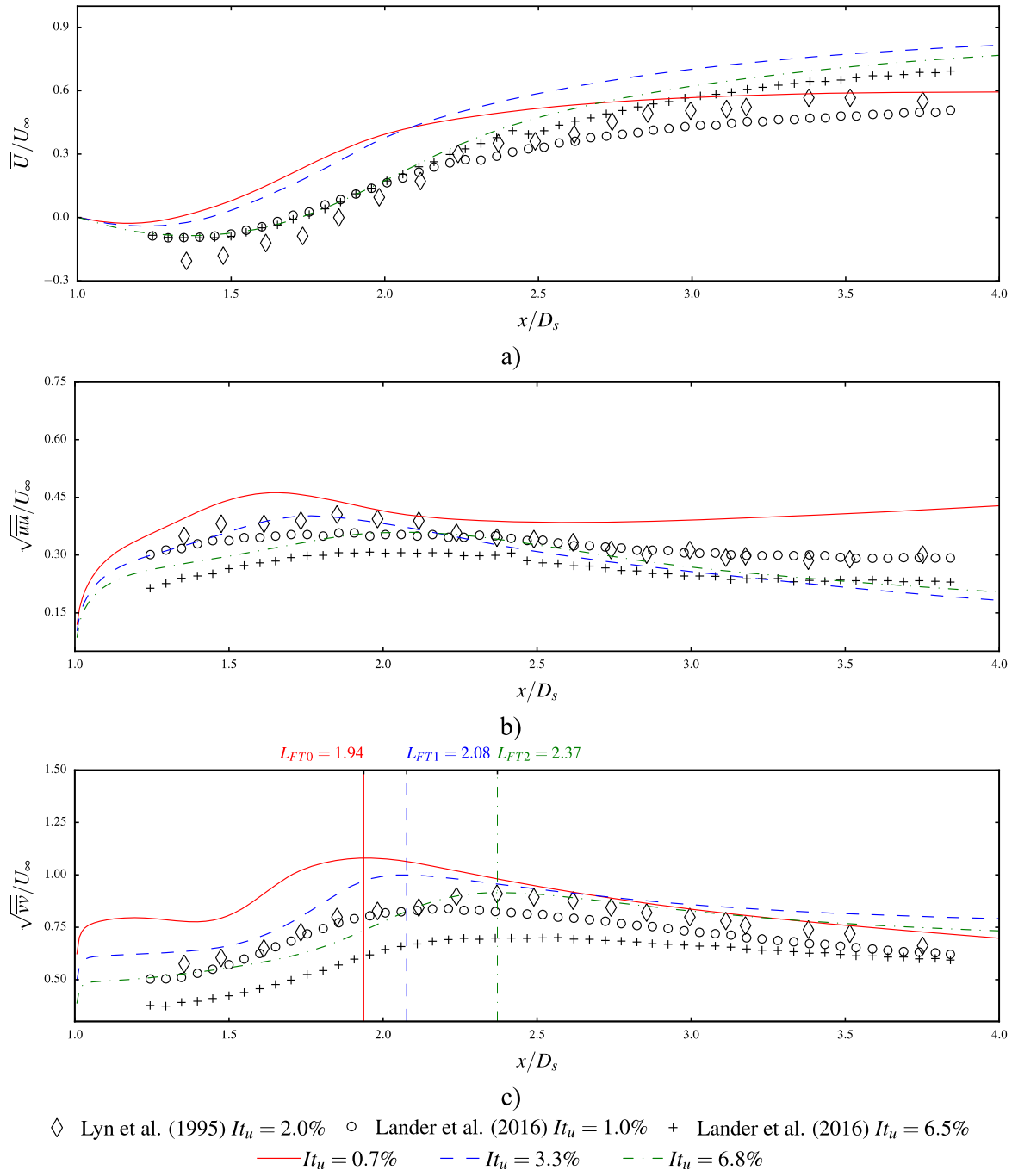

Fig. 11. Centerline downwind profiles of a) mean streamwise velocity, b) standard deviation of streamwise velocity and c) standard deviation of cross-stream fluctuating velocity components.

which is between the values obtained for T0 and T2.

In Fig. 12, for a set of near wall profiles located along the top side of the square prism, the numerical results obtained for the mean streamwise velocity and the Reynolds normal and shear stresses are presented along with experimental data (0.8% ambient FST in Minguez et al. (2011) and 2% FST in Lyn and Rodi (1994)).

For the mean streamwise velocity, the profiles obtained numerically within the range of considered FST levels are very similar among them, which agrees with the numerical results reported in Chen (2019). The comparison with experimental data is good, as the general shape of the profile and the region showing reverse flow are well captured. Only for the profiles located at $x/D_s = 0.625$ and 1 some discrepancies for the peak mean velocities with respect to the data in Minguez et al. (2011) can be identified.

For the streamwise Reynolds normal stress profiles, the numerical simulations show smaller peak values as the FST level is increased. For the ambient FST case T0, the qualitative agreement with the experimental data is good, providing the location of the peak values and even similar magnitudes, with the exception of the profile at $x/D_s = 0.25$. Similar comments apply for the T1 case when the results are compared with Lyn and Rodi (1994). According to experimental data, higher FST levels result in smaller peak values for the streamwise global Reynolds stresses, with the trend depicted by the 2D URANS simulations.

Analyzing the cross-stream global Reynolds normal stress profiles, the CFD results show a weak sensitivity with FST levels up to $x/D_s = 0.5$, providing peak magnitudes well below the experimental values in

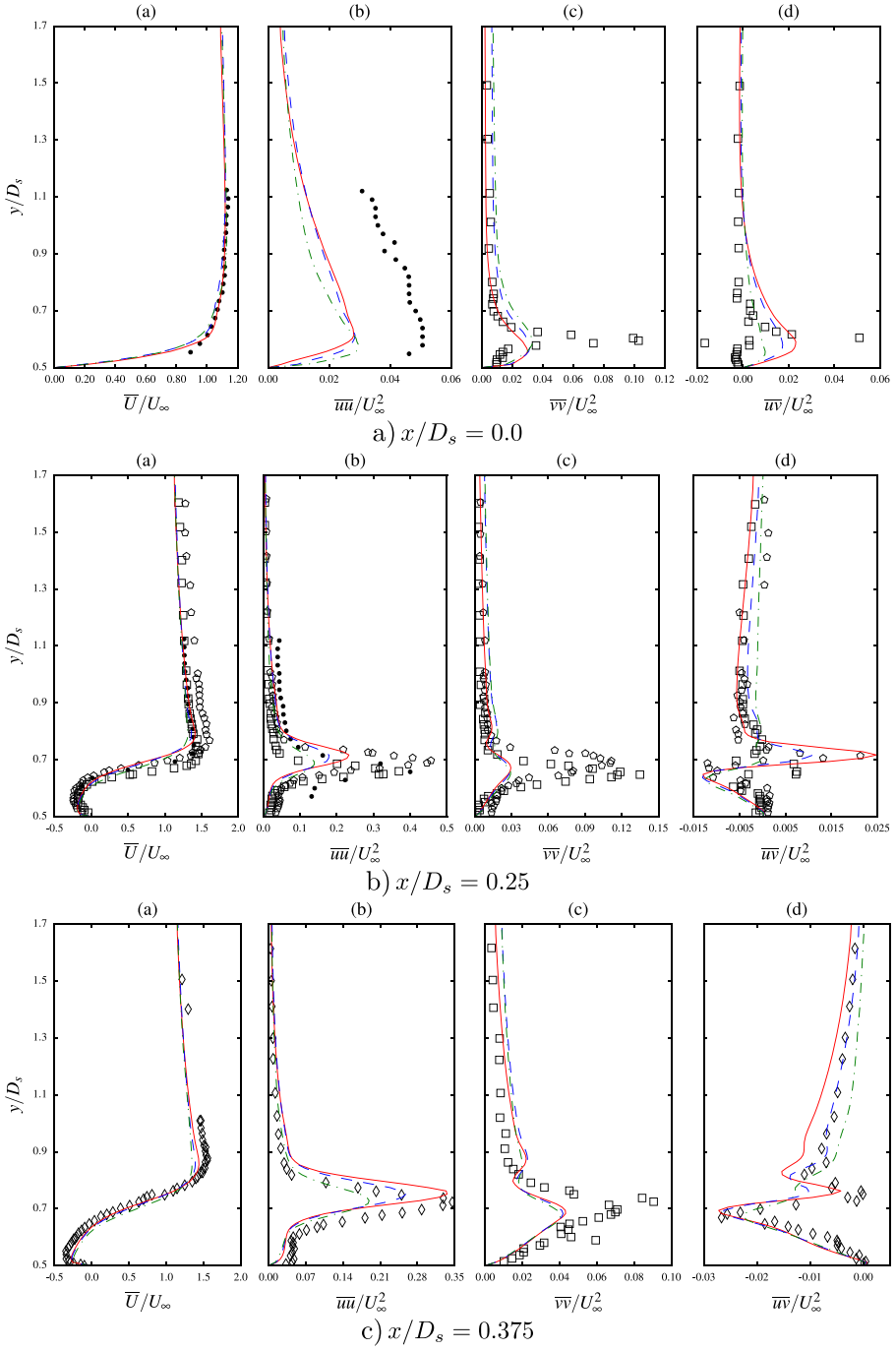

Minguez et al. (2011) $It_u < 0.8\%$	x/D_s						
	a)	b)	c)	d)	e)	f)	g)
□	0.1	0.2	0.4	0.5	0.6	0.7	0.9
⬠	-	0.3	-	-	-	0.8	-
◊	-	-	0.375	-	0.625	-	-

- Lyn and Rodi (1994) $It_u = 2.0\%$
- $It_u = 0.7\%$
- $It_u = 3.3\%$
- $It_u = 6.8\%$

Fig. 12a. Vertical profiles over the upper surface of the square prism (a) mean streamwise velocity, (b) streamwise, (c) cross-stream normal Reynolds stresses, and (d) the Reynolds shear stress.

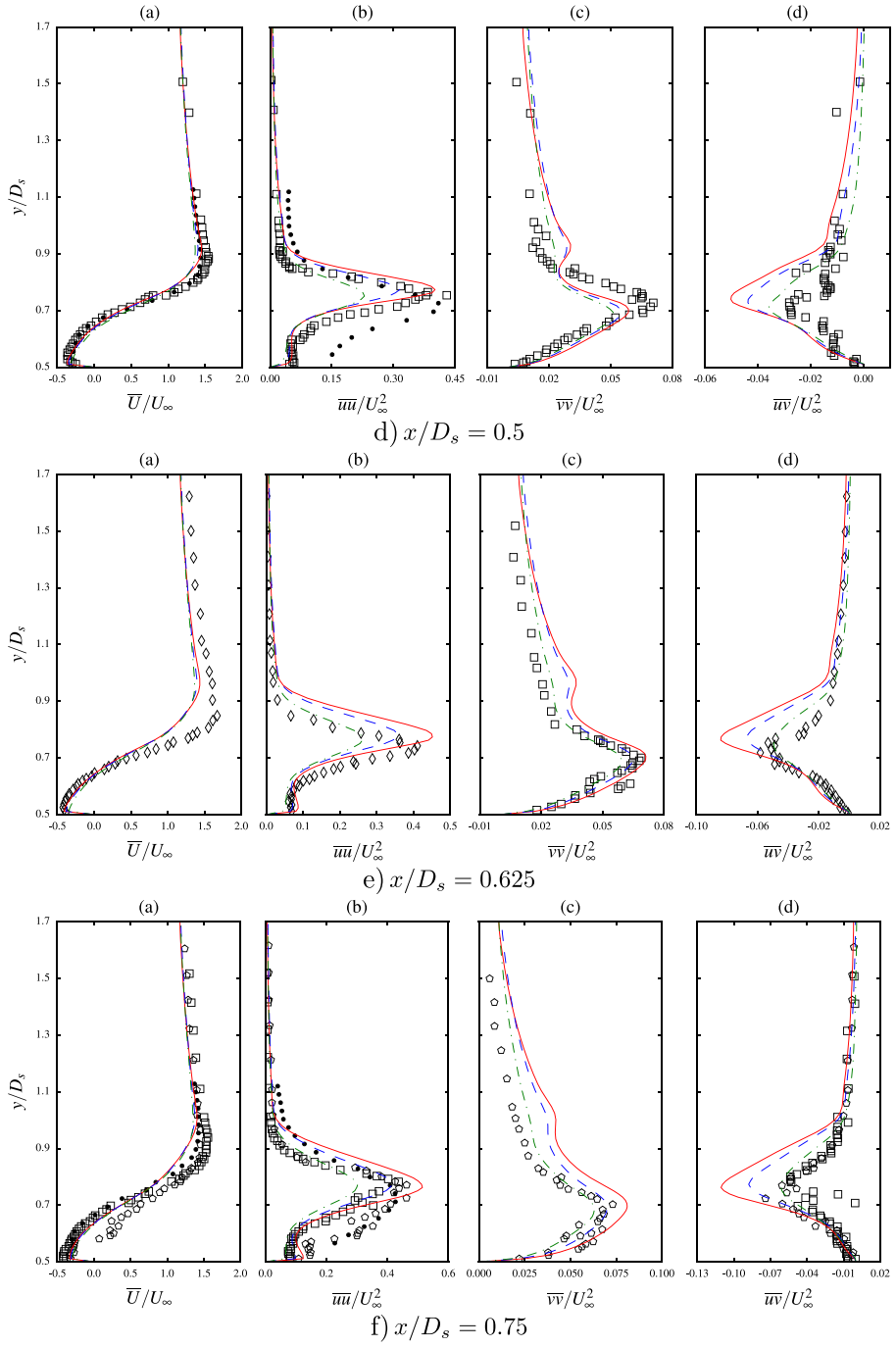

Minguez et al. (2011) $It_u < 0.8\%$	x/D_s						
	a)	b)	c)	d)	e)	f)	g)
□	0.1	0.2	0.4	0.5	0.6	0.7	0.9
⬠	-	0.3	-	-	-	0.8	-
◊	-	-	0.375	-	0.625	-	-

- Lyn and Rodi (1994) $It_u = 2.0\%$
- $It_u = 0.7\%$
- $It_u = 3.3\%$
- $It_u = 6.8\%$

Fig. 12b. Vertical profiles over the upper surface of the square prism (a) mean streamwise velocity, (b) streamwise, (c) cross-stream normal Reynolds stresses, and (d) the Reynolds shear stress (continued).

Minguez et al. (2011). Further downstream, in the CFD simulations higher FST levels are linked with smaller cross-stream Reynolds stresses close to the wall and the agreement with the experimental magnitudes certainly improves. In general, the profiles of cross-stream Reynolds stresses show a good qualitative agreement with the experimental data as the numerical results reproduce the general shape of the profile and the position of the peak values, although the peak values themselves are lower than the experimental values for $x/D_s < 0.5$.

Finally, for the profiles reporting the Reynolds shear stress, the agreement of the 2D URANS simulations is reasonable, capturing correctly the peak position and the general shape of the profiles, although in some cases higher negative peaks are reported. As the FST increases, the numerical simulation provides smaller values for the Reynolds shear stresses, which is in qualitative agreement with the

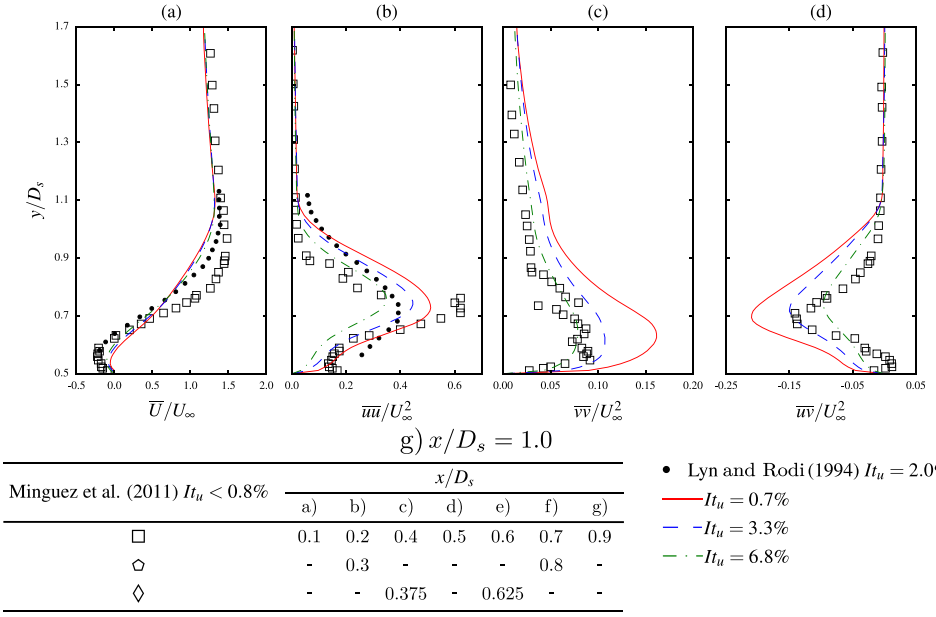

Fig. 12c. Vertical profiles over the upper surface of the square prism (a) mean streamwise velocity, (b) streamwise, (c) cross-stream normal Reynolds stresses, and (d) the Reynolds shear stress (continued).

experimental data reported in Lyn and Rodi (1994) and Minguez et al. (2011).

Overall, the ability of the proposed 2D URANS approach to replicate the fundamental flow features associated with FST effects on the aerodynamics of a square prism has been demonstrated. Not only the integral parameters have been correctly obtained for the different levels of FST, but complex features such as Reynolds stresses and mean streamwise velocity profiles have also been reproduced with a perhaps higher than expected level of accuracy.

6. Conclusions

The complexity and high computational burden of 3D LES simulations used in the numerical studies of FST has prompted the exploration of an alternative approach at a lower computational cost, to deliver at least qualitative agreement with experimental data. In this research, numerical simulations using a 2D URANS approach have been conducted in order to assess the feasibility of reproducing the effect of small-scale free stream turbulence in the aerodynamic response of a square prism. The desired FST level is achieved by locating a rod upstream of the prism, mimicking the procedure seldom used in wind tunnel testing to control the turbulence intensity level by varying the distance between the rod and the bluff body. This approach has proven to be an effective strategy to numerically reproduce the turbulence intensity levels reaching the bluff body.

One of the key issues in the numerical model has been the different characteristic length of the rod and the bluff body. Independent spatial and temporal verification studies were conducted for each geometry to identify the balanced grid and time step needed to produce accurate results for the study. In particular, the importance and convenience of analyzing the centerline wake profile of the rod-generated turbulence intensity in the verification study as well as in the preliminary validation of the numerical results are the cornerstone features of the proposed methodology.

The agreements between numerical results and available wind tunnel data have shed some lights on the feasibility of the proposed approach and its limitations. This relatively inexpensive 2D URANS strategy has been able to simulate the impact of different FST levels on the drag coefficient, mean and fluctuating pressure coefficient distributions, base pressure coefficient and mean flow features of a square prism. Furthermore, for fundamental aerodynamic features such as mean streamwise velocity profiles, fluctuating streamwise and cross-stream velocity components or Reynolds shear stress, the agreement of the numerical results with the experimental data has been generally good, reaching qualitative agreement and matching the experimental values in several cases.

This exploratory study has demonstrated the potential for the application of the proposed 2D URANS approach. Further research is needed to assess its feasibility and level of accuracy in more challenging problems, addressing the study of FST effects on the aeroelastic responses of bluff bodies as well as the aerodynamics and wind-induced responses of more complex geometries such as long-span bridges.

Declaration of competing interest

The authors declare that they have no known competing financial interests or personal relationships that could have appeared to influence the work reported in this paper.

Acknowledgements

Grant TED 2021-132243 B–I00 funded by the Ministry for Science and Innovation of Spain MCIN/AE/10.13039/501100011033 and by European Union NextGenerationEU/PRTR, and PID 2019-110786 GB-I00 funded by MCIN/AE/10.13039/501100011033, along with grants ED431C 2017/72 and ED431C 2021/33 funded by the Galician regional government.

The computations have been carried out in the computer cluster Breogan and in the Galician Supercomputation Technology Centre (CESGA).

The authors gratefully acknowledge the support received.

APPENDIX A

This method, proposed by Celik et al. (2008), is based on power expansion series, whose basic equation for estimation of the discretization error (ε) is:

$$\varepsilon_\phi \simeq \delta_{Re} = \phi_i - \phi_0 = \alpha h_i^{g_c}, \tag{A1}$$

where ϕ_i is the parameter for which the uncertainty is going to be calculated, ϕ_0 is the estimated exact solution, α is a constant, h is the representative cell size and g_c is the observed order of grid convergence.

In order to apply equation (A1), two assumptions must be fulfilled in accordance with Eça and Hoekstra (2014): the grids are inside the asymptotic range to guarantee that the leading term of the power series expansion is sufficient to estimate the error, and the level of refinement of the mesh can be represented by a single parameter, a representative cell size. This representative cell size is calculated as indicated by equation (A2).

$$h = \left[\frac{1}{N}\sum_{i=1}^{N}(\Delta V_i)\right]^{1/3}, \tag{A2}$$

where N is the overall number of elements and ΔV_i is the cell volume.

To apply this method, three meshes with increasing level of refinement are needed, therefore $h_1 < h_2 < h_3$, where 1 refers to the fine mesh and 3 to the coarse one. The provided meshes should present sufficiently different discretization levels. Hence, the grid refinement factor, defined as $r = h_3/h_1$, has to be greater than 1.3 (Celik et al., 2008).

The following equations show how the apparent order g_c of the method is calculated.

$$g_c = \frac{1}{ln\,(r_{21})}|ln|\varepsilon_{32}/\varepsilon_{21}| + q(g_c)|, \tag{A3}$$

$$q(g_c) = ln\left(\frac{r_{21}^{g_c} - s}{r_{32}^{g_c} - s}\right), \tag{A4}$$

$$s = 1\cdot sgn\left(\frac{\varepsilon_{32}}{\varepsilon_{21}}\right), \tag{A5}$$

$$r_{21} = h_2/h_1, r_{32} = h_3/h_2, \varepsilon_{21} = \phi_2 - \phi_1, \varepsilon_{32} = \phi_3 - \phi_2. \tag{A6}$$

If the ratio between the errors of the coarse mesh with respect the medium mesh, and between the medium and the fine mesh is negative $\left(\frac{\varepsilon_{32}}{\varepsilon_{21}} < 0\right)$, this is indicative of oscillatory convergence. The extrapolated values are calculated as indicated in equation (A7):

$$\phi_{ext}^{21} = (l_{21}^{g_c}\phi_1 - \phi_2)/(l_{21}^{g_c} - 1), \phi_{ext}^{32} = (l_{32}^{g_c}\phi_2 - \phi_3)/(l_{32}^{g_c} - 1) \tag{A7}$$

The method states that alongside with the apparent order of convergence g_c, the approximate relative error (e_a, see equation (A8)), the extrapolated relative error (e_{ext}, see equation 19) and the grid convergence index for the fine mesh (GCI_{fine}, see equation 20) has to be calculated and reported.

$$e_a^{21} = \left|\frac{\phi_1 - \phi_2}{\phi_1}\right|, \tag{A8}$$

$$e_{ext}^{21} = \left|\frac{\phi_{ext}^{12} - \phi_1}{\phi_{ext}^{12}}\right|, \tag{A9}$$

$$GCI_{fine}^{21} = \frac{1.25e_a^{21}}{r_{21}^{g_c} - 1}. \tag{A10}$$

Finally, the uncertainty for each grid is calculated as shown in equation (A11).

$$U_1 = \pm GCI_{fine}^{21}\phi_1. \tag{A11}$$

For further information about this method the interested reader is referred to the works of Celik et al. (2008) and Roache (2009).

APPENDIX B

Table B1
Spatial discretization uncertainty of the force coefficients and Strouhal number of the rod.[Ba]

	$\overline{C_d}$	$\overline{C_l}$	$\overline{C_m}$	$\tilde{C_d}$	$\tilde{C_l}$	$\tilde{C_m}$	St
N_1,N_2,N_3	507984, 180220, 84876						
h_1,h_2,h_3	2.486 $\times 10^{-2}$, 3.512 $\times 10^{-2}$, 4.513 $\times 10^{-2}$,						
r_{21}	1.413						
r_{32}	1.285						
ϕ_1	1.503	0.003	0.000	0.104	1.018	0.002	0.202
ϕ_2	1.514	0.030	0.000	0.129	1.141	0.003	0.199
ϕ_3	1.480	−0.001	0.000	0.099	1.012	0.002	0.236

(continued on next page)

Table B1 (*continued*)

	$\overline{C_d}$	$\overline{C_l}$	$\overline{C_m}$	$\widetilde{C_d}$	$\widetilde{C_l}$	$\widetilde{C_m}$	St
g_c	4.35	0.50	0.02	0.72	0.17	0.48	10.13
ϕ_{ext}^{21}	1.501	−0.139	0.064	0.018	−0.966	−0.002	0.202
ϕ_{ext}^{32}	1.531	0.262	−0.090	0.281	4.041	0.009	0.196
e_a^{21}	0.007	8.101	0.024	0.234	0.121	0.345	0.014
e_a^{32}	0.022	1.030	1.002	0.234	0.114	0.295	0.187
e_{ext}^{21}	0.002	1.024	1.000	4.843	2.055	2.091	0.0004
e_{ext}^{32}	0.011	0.886	0.995	0.542	0.718	0.698	0.016
GCI_{fine}^{21}	0.002	54.091	4.05×10^4	1.036	2.435	2.396	0.0005
GCI_{medium}^{32}	0.014	9.700	234.6	1.478	3.175	2.890	0.020
GCI_{coarse}	0.188	13.045	237.6	2.270	3.523	3.846	8.408
$\pm\, U_{fine}^{21} \times 10^3$	3.678	177.74	80.398	108.14	2479.9	4.895	0.109
$\pm\, U_{medium}^{32}$	0.021	0.290	0.111	0.190	3.624	0.008	0.004
$\pm\, U_{coarse}$	0.278	0.012	0.0002	0.224	3.564	0.007	1.987
Oscillatory convergence	yes	yes	yes	yes	yes	yes	yes

[Ba] N is the overall number of elements, h is the characteristic length size, r is the refinement ratio, g_c is the apparent order of the method, ϕ is the value of the variable of interest, ϕ_{ext} is the extrapolated value, e_a is the approximated relative error, e_{ext} is the extrapolated relative error, *GCI* is the grid convergence index, 1,2,3 refers to the fine, medium and coarse mesh respectively, and U is the uncertainty value.

Table B2
Spatial discretization uncertainty of the streamwise turbulence intensity.[Bb]

$x/\,D_s$	44.94	68.80	79.72	92.67	116.28	119.58	140.39	159.69	164.77
N_1,N_2,N_3	507984, 180220, 84876								
h_1,h_2,h_3	2.486×10^{-2}, 3.512×10^{-2}, 4.513×10^{-2}								
r_{21}	1.413								
r_{32}	1.285								
ϕ_1	0.072	0.058	0.054	0.050	0.045	0.044	0.041	0.038	0.037
ϕ_2	0.063	0.053	0.050	0.047	0.043	0.042	0.040	0.037	0.037
ϕ_3	0.047	0.042	0.040	0.039	0.037	0.036	0.035	0.033	0.033
g_c	3.02	3.56	3.50	4.18	4.96	5.09	6.27	8.11	8.75
ϕ_{ext}^{21}	0.076	0.061	0.056	0.051	0.045	0.045	0.041	0.038	0.037
ϕ_{ext}^{32}	0.076	0.061	0.056	0.051	0.045	0.045	0.041	0.038	0.037
e_a^{21}	0.123	0.094	0.087	0.067	0.045	0.043	0.027	0.015	0.012
e_a^{32}	0.246	0.213	0.191	0.175	0.144	0.140	0.121	0.108	0.105
e_{ext}^{21}	0.063	0.037	0.035	0.020	0.010	0.008	0.003	0.001	0.001
e_{ext}^{32}	0.178	0.128	0.119	0.086	0.055	0.051	0.030	0.016	0.013
GCI_{fine}^{21}	0.084	0.049	0.046	0.026	0.013	0.011	0.004	0.001	0.001
GCI_{medium}^{32}	0.271	0.184	0.169	0.118	0.073	0.068	0.039	0.020	0.016
GCI_{coarse}	1.642	1.539	1.366	1.426	1.398	1.405	1.666	2.542	3.024
$\pm\, U_{fine}^{21} \times 10^3$	5.999	2.841	2.498	1.313	0.561	0.494	0.177	0.046	0.029
$\pm\, U_{medium}^{32} \times 10^3$	17.031	9.727	8.383	5.554	3.113	2.864	1.553	0.758	0.604
$\pm\, U_{coarse}$	0.078	0.064	0.055	0.055	0.051	0.051	0.058	0.085	0.100
Oscillatory convergence	no	no	no	no	no	no	no	no	no

[Bb] N is the overall number of elements, h is the characteristic length size, r is the refinement ratio, g_c is the apparent order of the method, ϕ is the value of the variable of interest, ϕ_{ext} is the extrapolated value, e_a is the approximated relative error, e_{ext} is the extrapolated relative error, *GCI* is the grid convergence index, 1,2,3 refers to the fine, medium and coarse mesh respectively, and U is the uncertainty value.

Table B3
Spatial discretization uncertainty of the force coefficients and Strouhal number of the square prism.[Bc]

	$\overline{C_d}$	$\overline{C_l}$	$\overline{C_m}$	$\widetilde{C_d}$	$\widetilde{C_l}$	$\widetilde{C_m}$	St
N_1,N_2,N_3	478224, 169852, 80396						
h_1,h_2,h_3	2.536×10^{-2}, 3.582×10^{-2}, 4.596×10^{-2}						
r_{21}	1.412						
r_{32}	1.283						
ϕ_1	2.169	−0.003	−0.001	0.250	1.617	0.122	0.109
ϕ_2	2.191	−0.087	−0.015	0.210	1.558	0.118	0.112
ϕ_3	2.183	0.060	0.013	0.166	1.504	0.114	0.132
g_c	2.60	1.97	2.39	1.50	0.84	1.31	8.23
ϕ_{ext}^{21}	2.154	0.082	0.011	0.309	1.793	0.129	0.109
ϕ_{ext}^{32}	0.004	0.726	0.698	0.319	0.131	0.085	0.027
e_a^{21}	0.010	25.468	0.263	0.159	0.036	0.032	0.025

(*continued on next page*)

Table B3 (*continued*)

	$\overline{C_d}$	$\overline{C_l}$	$\overline{C_m}$	$\tilde{C_d}$	$\tilde{C_l}$	$\tilde{C_m}$	St
e_a^{32}	0.004	1.685	1.885	0.213	0.035	0.036	0.177
e_{ext}^{21}	0.007	1.040	1.051	0.190	0.098	0.054	0.002
e_{ext}^{32}	0.004	0.726	0.698	0.319	0.131	0.085	0.026
GCI_{fine}^{21}	0.009	32.552	25.690	0.294	0.135	0.071	0.002
GCI_{medium}^{32}	0.005	3.307	2.893	0.587	0.188	0.115	0.033
GCI_{coarse}	0.022	0.107	0.120	1.429	0.309	0.251	4.359
$\pm\ U_{fine}^{21} \times\ 10^3$	18.631	107.16	14.000	73.535	21.908	8.678	0.213
$\pm\ U_{medium}^{32}$	0.010	0.288	0.043	0.123	0.293	0.014	0.004
$\pm\ U_{coarse}$	0.048	0.639	0.158	0.237	0.465	0.029	0.573
Oscillatory convergence	yes	yes	yes	no	no	no	no

[Bc] N is the overall number of elements, h is the characteristic length size, r is the refinement ratio, g_c is the apparent order of the method, ϕ is the value of the variable of interest, ϕ_{ext} is the extrapolated value, e_a is the approximated relative error, e_{ext} is the extrapolated relative error, *GCI* is the grid convergence index, 1,2,3 refers to the fine, medium and coarse mesh respectively, and U is the uncertainty value.

Table B4
Temporal discretization uncertainty of the force coefficients and Strouhal number of the rod.[Bd]

	$\overline{C_d}$	$\overline{C_l}$	$\overline{C_m}$	$\tilde{C_d}$	$\tilde{C_l}$	$\tilde{C_m}$	St
h_1,h_2,h_3				0.5, 1.0, 2.0			
r_{21}				2.0			
r_{32}				2.0			
ϕ_1	1.503	0.003	0.000	0.104	1.018	0.002	0.202
ϕ_2	1.487	0.003	0.000	0.096	1.009	0.002	0.195
ϕ_3	1.438	0.001	0.000	0.079	0.972	0.002	0.180
g_c	1.57	1.66	1.00	1.01	1.97	0.24	1.01
ϕ_{ext}^{21}	1.501	−0.139	0.064	0.018	−0.966	−0.002	0.202
ϕ_{ext}^{32}	1.531	0.262	−0.090	0.281	4.041	0.009	0.196
e_a^{21}	0.011	0.173	1.000	0.080	0.009	0.049	0.036
e_a^{32}	0.033	0.661	∞	0.177	0.037	0.056	0.076
e_{ext}^{21}	0.005	0.074	0.500	0.073	0.003	0.384	0.035
e_{ext}^{32}	0.016	0.235	1.000	0.148	0.012	0.452	0.070
GCI_{fine}^{21}	0.007	0.100	1.250	0.099	0.004	0.347	0.045
GCI_{medium}^{32}	0.183	0.383	∞	0.217	0.016	0.389	0.094
GCI_{coarse}	0.183	3.818	∞	0.884	0.242	0.540	0.380
$\pm\ U_{fine}^{21} \times\ 10^3$	10.362	0.330	0.003	10.287	4.045	0.708	0.009
$\pm\ U_{medium}^{32}$	0.031	0.01	–	0.021	0.016	0.0008	0.018
$\pm\ U_{coarse}$	0.264	0.004	–	0.070	0.235	0.001	0.069
Oscillatory convergence	no	no	no	no	no	no	no

[Bd] h is the Courant number, r is the refinement ratio, g_c is the apparent order of the method, ϕ is the value of the variable of interest, ϕ_{ext} is the extrapolated value, e_a is the approximated relative error, e_{ext} is the extrapolated relative error, *GCI* is the grid convergence index, 1,2,3 refers to the short, regular and large mesh respectively, and U is the uncertainty value.

Table B5
Temporal discretization uncertainty of the streamwise turbulence intensity.[Be]

$x/\ D_s$	44.94	68.80	79.72	92.67	116.28	119.58	140.39	159.69	164.77
h_1,h_2,h_3					0.5, 1.0, 2.0				
r_{21}					2.0				
r_{32}					2.0				
ϕ_1	0.072	0.058	0.054	0.050	0.045	0.044	0.041	0.038	0.037
ϕ_2	0.072	0.059	0.055	0.051	0.045	0.045	0.041	0.038	0.038
ϕ_3	0.075	0.060	0.056	0.052	0.046	0.046	0.042	0.039	0.039
g_c	1.82	1.15	1.06	1.14	1.08	1.07	1.20	1.58	1.15
ϕ_{ext}^{21}	0.071	0.058	0.054	0.050	0.044	0.044	0.040	0.038	0.037
ϕ_{ext}^{32}	0.071	0.058	0.054	0.050	0.044	0.044	0.040	0.038	0.037
e_a^{21}	0.010	0.010	0.011	0.010	0.011	0.011	0.010	0.008	0.011
e_a^{32}	0.033	0.022	0.022	0.022	0.023	0.023	0.024	0.025	0.024
e_{ext}^{21}	0.004	0.008	0.010	0.009	0.010	0.010	0.008	0.004	0.008
e_{ext}^{32}	0.013	0.019	0.021	0.019	0.021	0.022	0.019	0.013	0.200
GCI_{fine}^{21}	0.005	0.010	0.012	0.011	0.012	0.013	0.010	0.005	0.011
GCI_{medium}^{32}	0.016	0.023	0.026	0.023	0.026	0.026	0.023	0.016	0.024

(*continued on next page*)

Table B5 (*continued*)

x/D_s	44.94	68.80	79.72	92.67	116.28	119.58	140.39	159.69	164.77
GCI_{coarse}	0205	0.112	0.111	0.112	0.116	0.117	0.123	0.141	0.121
$\pm U_{fine}^{21} \times 10^3$	0.338	0.609	0.678	0.536	0.552	0.563	0.416	0.201	0.416
$\pm U_{medium}^{32} \times 10^3$	1.193	1.348	1.411	1.179	1.169	1.184	0.956	0.603	0.926
$\pm U_{coarse}$	0.015	0.007	0.006	0.006	0.005	0.005	0.005	0.005	0.005
Oscillatory convergence	no	no	no	no	no	no	no	no	no

[Be] h is the Courant number, r is the refinement ratio, g_c is the apparent order of the method, ϕ is the value of the variable of interest, ϕ_{ext} is the extrapolated value, e_a is the approximated relative error, e_{ext} is the extrapolated relative error, *GCI* is the grid convergence index, 1,2,3 refers to the short, regular and large mesh respectively, and U is the uncertainty value.

Table B6
Temporal discretization uncertainty of the force coefficients and Strouhal number of the square prism.[Bf]

	$\overline{C_d}$	$\overline{C_l}$	$\overline{C_m}$	$\tilde{C_d}$	$\tilde{C_l}$	$\tilde{C_m}$	St
h_1,h_2,h_3				0.5, 1.0, 2.0			
r_{21}				2.0			
r_{32}				2.0			
ϕ_1	2.169	−0.003	−0.001	0.250	1.617	0.122	0.109
ϕ_2	2.149	0.036	0.007	0.245	1.613	0.121	0.107
ϕ_3	2.129	−0.005	−0.001	0.247	1.605	0.119	0.105
g_c	0.03	0.07	0.08	1.15	0.95	0.67	0.50
ϕ_{ext}^{21}	3.030	−0.835	−0.140	0.255	1.622	0.124	0.113
ϕ_{ext}^{32}	3.030	0.907	0.155	0.243	1.622	0.124	0.113
e_a^{21}	0.009	12.041	14.349	0.022	0.003	0.010	0.014
e_a^{32}	0.010	1.143	1.135	0.010	0.005	0.015	0.020
e_{ext}^{21}	0.284	0.996	0.996	0.018	0.003	0.016	0.033
e_{ext}^{32}	0.291	0.960	0.953	0.008	0.005	0.025	0.046
GCI_{fine}^{21}	0.496	315.65	320.22	0.022	0.003	0.020	0.042
GCI_{medium}^{32}	0.512	29.953	25.333	0.010	0.007	0.032	0.061
GCI_{coarse}	0.536	32.878	28.250	0.051	0.025	0.081	0.121
$\pm U_{fine}^{21} \times 10^3$	1076.0	1039.1	174.52	5.603	5.570	2.444	4.606
$\pm U_{medium}^{32}$	1.101	1.089	0.184	0.003	0.002	0.005	0.0004
$\pm U_{coarse}$	1.142	0.170	0.028	0.013	0.040	0.010	0.013
Oscillatory convergence	no	yes	yes	yes	no	no	no

[Bf] h is the Courant number, r is the refinement ratio, g_c is the apparent order of the method, ϕ is the value of the variable of interest, ϕ_{ext} is the extrapolated value, e_a is the approximated relative error, e_{ext} is the extrapolated relative error, *GCI* is the grid convergence index, 1,2,3 refers to the short, regular and large mesh respectively, and U is the uncertainty value.

References

Alvarez, A.J., Nieto, F., Kwok, K.C.S., Hernández, S., 2018. Aerodynamic performance of twin-box decks: a parametric study on gap width effects based on validated 2D URANS simulations. J. Wind Eng. Ind. Aerod. 182, 202–221.

Alvarez, A.J., Nieto, F., Kwok, K.C.S., Hernández, S., 2021. Square cylinder under different turbulent intensity conditions by means of small-scale turbulence. In: Proc. Of the 11th International Conference on Advances in Fluid Dynamics with Emphasis on Multiphase and Complex Flow (AFM/MPF 21), vol. 132, pp. 103–114. WIT Transactions on Engineering Sciences.

Balduzzi, F., Zini, M., Ferrara, G., Bianchini, A., 2019. Development of a CFD methodology to reproduce the effects of macro turbulence on wind turbines and its application to the particular case of a VAWT. In: In Proceedings of ASME Turbo Expo 2019: Turbomachinery Technical Conference and Exposition (Phoenix, Arizona, USA).

Bervida, M., Patruno, L., Stanic, S., de Miranda, S., 2020. Synthetic generation of the atmospheric boundary layer for Wind loading assessment using spectral methods. J. Wind Eng. Ind. Aerod. 196, 104040.

Bruno, L., Oberto, D., 2022. Effects of cell quality in grid boundary layer on the simulated flow around a square cylinder. Comput. Fluid 238 paper ID 105351.

Bruno, L., Khris, S., 2003. The validity of 2D numerical simulations of vertical structures around a bridge deck. Math. Comput. Model. 37, 795–828.

Bruno, L., Salvetti, M.V., Ricciardelli, F., 2014. Benchmark on the Aerodynamics of a rectangular 5:1 cylinder: an overview after the first four years of activity. J. Wind Eng. Ind. Aerod. 126, 87–106.

Cao, Y., Tamura, T., 2015. Numerical investigations into effects of three-dimensional wake patterns on unsteady aerodynamic characteristics of a circular cylinder at Re=1.3×105. J. Fluid Struct. 59, 351–369.

Carassale, L., Freda, A., Marrè-Brunenghi, M., 2013. Effects of free-stream turbulence and corner shape on the galloping instability of square cylinders. J. Wind Eng. Ind. Aerod. 123, 274–280.

Celik, I.B., Ghia, U., Roache, P.J., Freitas, C.J., Coleman, H., Raad, P.E., 2008. Procedure for estimation and reporting of uncertainty due to discretization in CFD applications. J. Fluid Eng. 130 (7), 78001-1-4.

Chen, Y., 2019. Aerodynamics of Smooth and Turbulent Flows Past Stationary and Oscillating Square Cylinders. Ph.D. thesis). University of Southampton.

Chen, Y., Djidjeli, K., Xie, Z.T., 2020. Large eddy simulation of flow past stationary and oscillating square cylinders. J. Fluid Struct. 97 paper ID: 103107.

Daniels, S.J., Castro, I.P., Xie, Z.T., 2016. Numerical analysis of freestream turbulence effects on the vortex-induced vibrations of a rectangular cylinder. J. Wind Eng. Ind. Aerod. 153, 13–25.

Eça, L., Hoekstra, M., 2014. A procedure for the estimation of the numerical uncertainty of CFD calculations based on grid refinement studies. J. Comput. Phys. 262, 104–130.

Farell, C., Iyengar, A.K.S., 1999. Experiments on the wind tunnel simulation of atmospheric boundary layers. J. Wind Eng. Ind. Aerod. 79, 11–35.

Gartshore, I.S., 1973. The Effects of the Free Stream Turbulence on the Drag of Rectangular Two-Dimensional Prisms. University of Western Ontario, Canada. Technical report BLWT-4-T3.

Haque, N., Katsuchi, H., Yamada, H., Nishio, M., 2014. Investigation of flow fields around rectangular cylinder under turbulent flow by LES. Engineering Applications of Computational Fluid Mechanics 8, 396–406.

Hussain, A.K.F., Reynolds, W.C., 1972. The mechanics of an organized wave in turbulent shear flow. Part 2. Experimental results. J. Fluid Mech. 54, 241.

Kiya, M., Sasaki, K., 1983. Free-stream turbulence effects on a separation bubble. J. Wind Eng. Ind. Aerod. 14, 375–386.

Klein, M., Sadiki, A., Janicka, J., 2003. A digital filter based generation of inflow data for spatially developing direct numerical simulation or large eddy simulation. J. Comput. Phys. 186, 652–665.

Kozmar, H., Laschka, B., 2019. Wind-tunnel modelling of wind loads on structures using truncated vortex generators. J. Fluid Struct. 87, 334–353.

Kwok, K.C.S., 1986. Turbulence effect on flow around circular cylinder. J. Eng. Mech. 112 (11), 1181–1197. Paper No. 21029.

Kwok, K.C.S., Melbourne, W.H., 1980. Freestream turbulence effects on galloping. EM2 J. Eng. Mech. Div. 106, 273–288. Paper No. 15356.
Lander, D.C., Letchford, C.W., Amitay, M., Kopp, G.A., 2016. Influence of the bluff body shear layers on the wake of a sqsuare prism in a turbulent flow. Phys. Rev. Fluids 1, 044406.
Lee, B.E., 1975. The effect of turbulence on the surface pressure field of a square prims. J. Fluid Mech. 69 (2), 263–282.
Li, M., Li, Q., Shi, H., Li, M., 2022. Effects of free-stream turbulence on the near wake flow and aerodynamic forces of a square cylinder. J. Fluid Struct. 114, 103748.
Li, Q.S., Hu, G., Yan, B.W., 2014. Investigation of the effects of free-stream turbulence on wind-induced responses of tall building by large eddy simulation. Wind and Structures, An International Journal 18 (6), 599–618.
Liu, Z., 2012. Investigation of flow characteristics around square cylinder with inflow turbulence. Engineering Applications of Computational Fluid Mechanics 6 (3), 426–446.
Lund, T., Wu, X., Squires, D., 1998. Generation of turbulent inflow data for spatially developing boundary layer simulation. J. comp. Phys. 140, 233–258.
Lyn, D.A., Einav, S., Rodi, W., Park, J.-H., 1995. A laser-Doppler velocimetry study of ensemble-averaged characteristics of the turbulent near wake of a square cylinder. J. Fluid Mech. 304, 285–319.
Lyn, D.A., Rodi, W., 1994. The flapping shear layer formed by flow separtion from the forward corner of a square cylinder. J. Fluid Mech. 267, 353–376.
McLean, I., Gartshore, I., 1992. Spanwise correlations of pressure on a rigid square section cylinder. J. Wind Eng. Ind. Aerod. 41 (1–3), 797–808.
Menter, F., 2009. Review of the shear-stress transport turbulence model experience from an industrial perspective. Int. J. Comput. Fluid Dynam. 23 (4), 305–316.
Menter, F., Esch, T., 2001. Elements of industrial heat transfer prediction. In: Proc. Of the 16th Brazilian Congress on Mechanical Engineering.
Minguez, M., Brun, C., Pasquetti, R., Serre, E., 2011. Experimental and high-order LES analysis of the flow in near-wall región of a square cylinder. Int. J. Heat Fluid Flow 32, 558–566.
Mochida, A., Murakami, S., Shoji, M., Ishida, Y., 1993. Numerical simulation of flow field around Texas Tech Building by large eddy simulation. J. Wind Eng. Ind. Aerod. 46–47, 455–460.
Moukalled, F., Mangani, L., Darwish, M., 2016. The finite volume method in Computational Fluid Dynamics. In: Fluid Mechanics and its Applications Series, vol. 113 (Springer).
Nakamura, Y., Ohya, Y., 1986. Vortex shedding from square prisms in smooth and turbulent flows. J. Fluid Mech. 164, 77–89.
Noda, H., Nakayama, A., 2003. Reproducibility of flow past two-dimensional rectangular cylinders in a homogeneous turbulent flow by LES. J. Wind Eng. Ind. Aerod. 91, 265–278.
Oberkampf, W.F., Roy, C.J., 2010. Verification and Validation in Scientific Computing. Cambridge University Press, Cambridge, UK.
Patruno, L., Ricci, M., 2018. A systematic approach to the generation of synthetic turbulence using spectral methods. Comput. Methods Appl. Mech. Eng. 340, 881–904.
Ranjan, P., Dewan, A., Kumar, S., 2017. Effect of free-stream turbulence on fluid flow and heat transfer from square cylinder. HEFAT2017. 17-19 July. In: Proc. 13th International Conference on Heat Transfer, Fluid Mechanics and Thermodynamics. Portorz, Slovenia.
Ricci, M., Patruno, L., de Miranda, S., Ubertini, F., 2017. Flow field around a 5:1 rectangular cylinder using LES: influence of inflow turbulence conditions, spanwise domain size and their interaction. Comput. Fluid 149, 181–193.
Roache, P.J., 2009. Fundamentals of verification and validation. Hermosa, Socorro, New Mexico.
Saathoff, P.J., Melbourne, W.H., 1989. The generation of peak pressures in separated/reattaching flows. J. Wind Eng. Ind. Aerod. 32, 121–134.
Tamura, T., Ono, Y., 2003. LES analysis on aeroelastic instability of prisms in turbulent flow. J. Wind Eng. Ind. Aerod. 91, 1827–1846.
Tang, S.L., Antonia, R.A., Djenidi, L., Zhou, Y., 2016. Complete self-preservation along the axis of a circular cylinder far wake. J. Fluid Mech. 786, 253–274.
Townsend, A., 1949. Momentum and energy diffusion in the turbulent wake of a cylinder. Proc. Roy. Soc. 197, 124.
Vickery, B.J., 1966. Fluctuating lift and drag on a long cylinder of square cross-section in a smooth and in a turbulent stream. J. Fluid Mech. 25, 481–494.
Vita, G., Hemida, H., Andrianne, T., Charalampos, C., Baniotopoulos, C., 2018. Generating atmospheric turbulence using pasive grids in an expansión test section of a wind tunnel. J. Wind Eng. Ind. Aerod. 178, 91–104.
Wilcox, D.C., 2006. Turbulence Modelling for CFD, third ed. DCW Industries Inc.
Wu, X., 2017. Inflow turbulence generation methods. Annu. Rev. Fluid Mech. 49, 23–49.
Xie, Z.T., Castro, I.P., 2008. Efficient generation of inflow conditions for Large Eddy Simulation of stree-scale flows. Flow, Turbul. Combust. 81 (3), 449–470.
Xing, J., Patruno, L., Pozzuoli, C., Pedro, G., de Miranda, S., Ubertini, F., 2022. Wind loads prediction using LES: inflow generation, accuracy and cost assessment for the case of Torre Gioia 22. Eng. Struct. 262, 114292.
Yu, R., Bay, X.S., 2014. A fully divergence-free method for generation of inhomogeneous and anisotropic turbulence with large spatial variation. J. Comput. Phys. 256, 234–253.
Zhao, C., Wang, H., Zeng, L., Alam, M.M., Zhao, X., 2021. Effects of oncoming flow turbulence on the near wake and forces of a 3D square cylinder. J. Wind Eng. Ind. Aerod. 214 paper ID. 104674.
Zhu, G., Huang, S., Li, Q.S., 2020. Large-eddy simulation of the inflow turbulence transport and aerodynamics of a rectangular 5:1 cylinder with high-order numerical methods. J. Wind Eng. Ind. Aerod. 207, 104366.